Thermocapillary Effects on Fluid Distributed on Wettability-Confined Tracks

BY

ANTONIO LAFRATTA
B.S, Politecnico di Torino, Turin, Italy, 2015

THESIS

Submitted as partial fulfillment of the requirements
for the degree of Master of Science in Mechanical Engineering
in the Graduate College of the
University of Illinois at Chicago, 2017

Chicago, Illinois

Defense Committee:

Constantine M. Megaridis, Chair and Advisor
Jie Xu
Pietro Asinari, Politecnico di Torino

To my father and my mother,

for all the battles they have won, and for all the battles they are going to win.

To Maria,

for what she was, for what she is, and for what she will always be for me.

To my brother Andrea.

ACKNOWLEDGMENTS

First and foremost, I would like to express my sincere gratitude to Prof. Constantine M. Megaridis, whose strong personality and attitude to work have motivated me to do always my best. Furthermore, I want to thank Prof. Pietro Asinari for his advices and his support during this entire period.

My deepest gratitude goes to Theo, who helped me every single day I have worked on this project and without whom I would have never completed it. Many thanks also to Mohamed, Jared, Reza, Ali, Aritra, Uddalok, Pat and Souvick, for their precious hints and for all the fun times we have had in the lab. I also thank Unmeelan and Alfredo for having been my great roomates, as well as my everyday mates Enrico, Marco, Chiara and Simone.

Thanks to Martina, for the happiness she brought into my life. Moreover, I want to thank my greatest friends Francesco and Andrea for being always by my side, as well as all the other guys I have known in Turin, whose friendship is one of the most precious things I have obtained during these five years spent away from home. Finally, my utmost gratitude goes to my parents, who always supported me from the beginning and to whom I will be grateful for the rest of my life.

AL

TABLE OF CONTENTS

TABLE OF CONTENTS (continued)

CHAPTER **PAGE**

LIST OF TABLES

LIST OF FIGURES

LIST OF FIGURES (continued)

FIGURE **PAGE**

LIST OF SYMBOLS AND ABBREVIATIONS

CA	Contact angle
Bi	Biot number
Bo	Bond number
k	Thermal conductivity
h	Heat transfer coefficient

Greek letters

γ	Surface tension
κ^{-1}	Capillary length
ρ	Density
τ	Shear stress

SUMMARY

The study of the thermocapillary effect on a silicone oil distributed on wedge-shaped and straight wettability-confined tracks has been hereafter conducted in order to demonstrate the effective mass transfer, due to a surface tension gradient, when a change in the thermal conditions of the system is provided.

A superoleophilic track on an oleophobic background provides the means to confine the fluid on an appropriate steel sample, whilst a compact insulating setup is meant to accomodate the steel plate and to impart a specific temperature gradient by means of two Peltier micro modules.

The distortion of the shape of the oil has been visualized and analyzed for both types of tracks, by using shadow photography and image processing with appropriate softwares. Globally, the effects of the Laplace pressure and gravity have been found to have a strong consequence when wedge-shaped tracks are considered, thus acting against the thermocapillary force.

Furthermore, the importance of the track length, which seems to play a huge role in preventing the fluid movement when straight tracks are analyzed, has been noted and recorded, thus preparing a future study designed to produce more detailed results.

CHAPTER 1

CAPILLARITY

The study of capillarity in liquids was first evaluated during the earliest part of the 19th century by Thomas Young (1773 - 1829) and Pierre Simon de Laplace (1749 - 1827), whose work was later unified by the German mathematician Carl Friedrich Gauss (1777 - 1855) in order to derive the basic equations that describe this phenomenon.

The analysis of the interfaces between two liquids, or even between air and a certain liquid, is what it is called capillarity. Every interface is deformable and thus free to modify its shape with the aim of minimizing its surface energy. Moreover, capillarity plays an important role in scientific research (surface physics, climate, biology) and in the industry (automotive, chemical, textile and more).

1.1 Surface tension

Every liquid, which is technically defined as a condensed state composed of molecules that attract one another, can flow quickly adopting very stable shapes, with the surface that can be thought to be similar to a streched membrane affected by a surface tension that counteracts its distortion; therefore if the thermal agitation of molecules is weaker than their attraction, a change from a gas phase to a liquid phase happens.

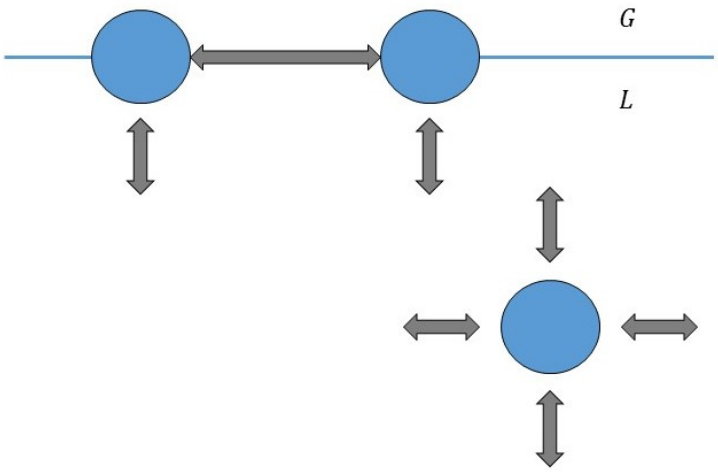

Figure 1: Cohesive forces between molecules at the surface and in the bulk of a liquid

Each molecule set in the bulk of a liquid is subjected to an interaction force shared with all neighboring molecules, that is mainly a cohesive force; on the other hand, molecules on the surface do not have other molecules above and show stronger attractive forces upon the closest neighbors on the surface (Figure 1). This strengthening of the intermolecular attractive forces leads to the origins of surface tension.

A liquid molecule on the surface is thus characterized by an unfavorable energy state. If U is the cohesion energy of a molecule placed within a liquid, the corresponding energy of another molecule sitting at the surface is roughly $U/2$, which creates an energy deficit that can be used to estimate the surface tension in a direct way. By calling b the size of the molecule and b^2 its

TABLE I: SURFACE TENSION OF SELECT LIQUIDS AT 20°C

Liquid	Surface tension γ (mN/m)
Water	73
Silicone Oil	20.8
Ethanol	23
Hexadecane	18.43
Mercury	485
Benzene	28

exposed area, the surface tension can be easily computed as $\gamma \cong U/(2b^2)$. Due to the presence of hydrogen bonds in a water molecule, the value of its surface tension is higher than most common oils, which present Van der Waals type bonds.

Some values of the surface tension of a few ordinary liquids are presented in Table I. It is observed that γ may be expressed both in J/m^2 and in N/m, as explained in the next paragraph.

1.1.1 Mechanical definition

Imagine now the increase of the surface area of a liquid by an amount dA in order to distort its structure, thus supplying a certain amount of energy.

The work required is a function of the amount of molecules that need to be raised to the surface:

$$\delta W = \gamma dA \tag{1.1}$$

where γ is the liquid surface tension.

The dimensional analysis of this equation gives $[\gamma] = EL^{-}2$, where E defines the work (or

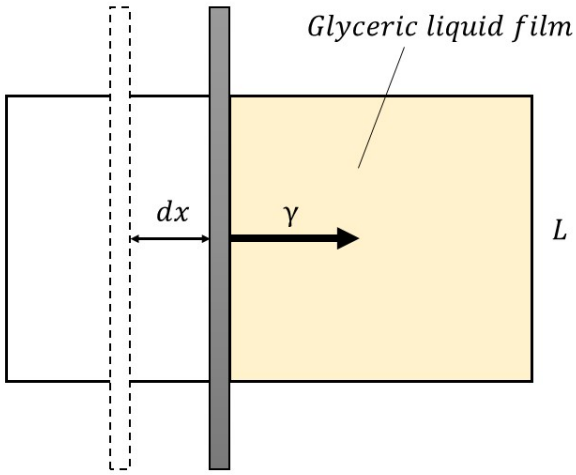

Figure 2: Top view of the rectangular apparatus after its removal from the liquid mixture: the yellow part represents the soapy solution in which the rectangular glass rod is immersed, which creates a very thin film delimited by three sides of the rod and by the additional movable rod which constitutes the fourth side of the rectangle.

energy), determined as ML^2T^2 in terms of fundamental quantities, which means that γ is expressed in J/m^2. The following definition is adopted, which states that "γ *is the energy that must be supplied to increase the surface area by one unit.*" [1]

Moreover, surface tension can be seen as a force per unit length, since it can be expressed in N/m; dimensionally, it can be written $[\gamma] = FL^{-}1$, where F is related to the fundamental quantities as $MLT^{-}2$.

As an example of how γ behaves as a force, we consider a rectangular glass rod with the short side of length L, onto which another rod is placed (Figure 2), the latter being free to trundle on the borders of the rectangle, immersed into a liquid containing glycerine, bubble soap and water; once it is removed from the mixture, one can see a natural movement towards the right so as to diminish the liquid surface area, whih allows to compute the work done by the rod, supposing that it moves by a range dx:

$$\delta W = Fdx = 2\gamma Ldx \tag{1.2}$$

in which the coefficient 2 highlights the two interfaces in the system. In this way, γ is demonstrated to be a force per unit length of the rod directed toward the liquid.
This concept is the basis for the understanding of the capillary forces which, for example, allows insects to be in equilibrium on water without drowning (Figure 3).

1.1.2 Laplace pressure

Surface tension also explains the presence of the overpressure inside bubbles and drops which, for instance, leads big drops in an emulsion to outlast smaller ones or produces the phenomenon of the capillary adhesion between a pair of plates. The jump in pressure that

Figure 3: Capillary forces enable insects to walk on water (Source: http://seawayblog.blogspot.com/2009/05/color-water-insects.html)

occurs across a curved surface or interface can be explained by means of Laplace's theorem, which is now presented as a general concept valid for any surface.

Laplace's theorem:

"*The increase in hydrostatic pressure* Δp *that occurs upon traversing the boundary between two fluids is equal to the product of the surface tension* γ *and the curvature of the surface* $C = \frac{1}{R} + \frac{1}{R'}$" [1]:

$$\Delta p = \gamma \left(\frac{1}{R} + \frac{1}{R'} \right) = \gamma C \tag{1.3}$$

where R and R' denote the principal radii of curvature of the surface.

As an example, Figure 5 shows water (w) containing a small drop of oil (o), the latter assuming a spherical configuration of radius R in order to reduce its surface energy, by which

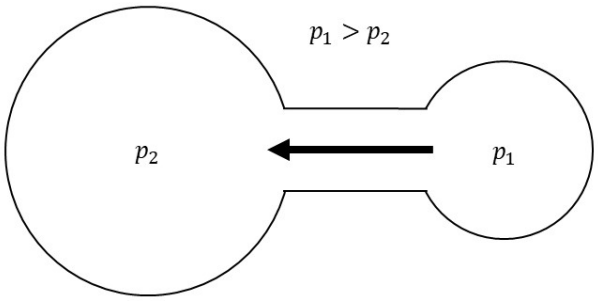

Figure 4: Larger bubbles absorb small ones

it is possible to compute the work done both by the capillary force and the pressure when the interface between water and oil is shifted by dR:

$$\delta W = -p_o dV_o - p_w dV_w + \gamma_{ow} dA \tag{1.4}$$

where $dV_o = 4\pi R^2 dR = -dV_w$ is the drop's increase in volume, $dA = 8\pi R dR$ its increase in surface, γ_{ow} represents the interfacial tension among water and oil, while p_w and p_o stand for

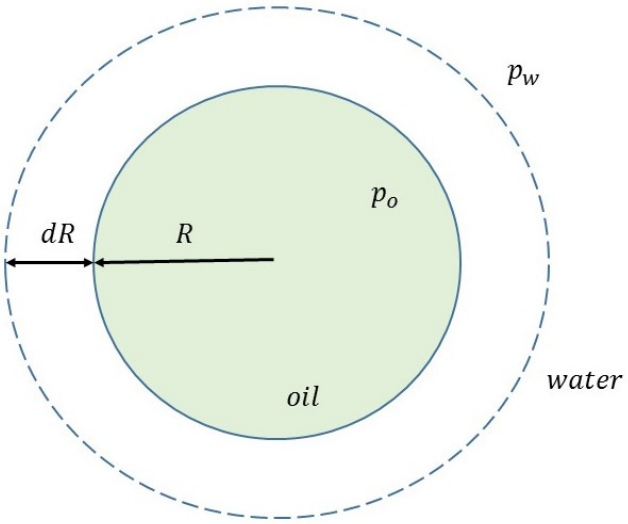

Figure 5: Overpressure of oil in water

the pressures in the water and oil respectively. By setting $\delta W = 0$, the condition for mechanical equilibrium is satisfied and the equation becomes:

$$\Delta p = p_o - p_w = \frac{2\gamma_{ow}}{R} \tag{1.5}$$

Therefore, a bigger inner pressure is achieved if the drop is very small, a phenomenon visible in soap bubbles where the smaller bubbles empty themselves into the larger ones (Figure 4).

1.2 Wetting

The phenomenon of wetting is referred to as the condition for which a liquid tends to spread once it is placed on a solid or on another liquid. Numerous industrial applications in which wetting plays an important role can be found, such as: treatment of tires to create adhesion on roadways or preparation of the surface before painting in automobile manufacturing; ink and paints in the chemical industry; powders like cocoa in the food industry; waterproofing of concrete and treatment of plastic in civil engineering.

It is also worth to take into account the role of wetting in the life sciences: surfactant molecules which start the inflation of lungs by lowering their surface energy; ability of insects to walk on water; wetting of eyes.

Two types of wetting will be analyzed, the total wetting (the liquid covers the whole solid) and similarly, the partial wetting. However, before going on with this analysis and in order to better understand the phenomena and the terms that will be presented, a brief section is dedicated to the terminology employed to rank surfaces according to their wettability by liquids, soon after the explanation of the physics and the forces that govern this phenomenon.

1.2.1 Partial and total wetting

According to the type of surface a water drop is put on, one can see a situation of complete spreading or, by contrast, the drop stays steady at a point. Whereby, there will be two different

wetting regimes, described by the *spreading parameter* S that estimates the gap in between the surface energy (per unit area) of the dry substrate and the wet one:

$$S = E_{s,dry} - E_{s,wet} \tag{1.6}$$

or in another form:

$$S = \gamma_{SA} - (\gamma_{SL} + \gamma) \tag{1.7}$$

in which γ is the surface energy at the liquid/air interface, γ_{SA} the surface energy at the solid/air interface and γ_{SL} the one at the solid/liquid interface (Figure 6).

When the spreading parameter is positive, a decrease of the liquid surface energy is achieved by a complete distribution of the drop on the solid which creates a very small thickness film, driven by the balance between molecular and capillary force. Viceversa, if S is negative, the drop does not spread and sits on the substrate highlighting a well-defined contact angle θ_C obtainable by projecting the three surface tensions on the plane, as shown in Figure 6.

The equilibrium of the three forces gives the following balance equation:

$$\gamma_{SA} = \gamma_{SL} + \gamma cos\theta_C \tag{1.8}$$

If the value of θ_C is lower than $\pi/2$, the liquid tends to cover the substrate and thus to be "mostly wetting", whilst if θ_C is higher than $\pi/2$ the liquid is said to be "mostly non-wetting". The value $\theta_C = 0$ refers to a transition condition, while $\theta_C = \pi/2$ does not have any notable

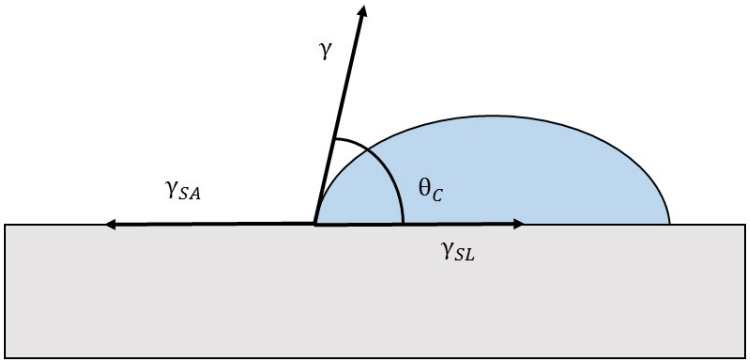

Figure 6: Balance of surface tensions

role from a thermodynamical point of view [3].

1.2.2 Terminology of wettability

When the study of wettability is taken into account, terms such as "hydrophilic" and "hydrophobic" are commonly referred to in the majority of applications in which liquids covering solid surfaces are considered, as well as to their classification in terms of solubility in water. [2] In addition, other words such as "oleophobic(philic)" or "hygrophobic(philic)" are introduced when liquids different from water are involved.

Since the terms "hydro", "philic" and "phobic" derive from the three Greek words for water, love and fear, they can be generally referred to describe any relation between water and other materials.

However, the specific function or process should always be defined if these words are to be used, since the number of operations in which wetting is involved is very large. [2]

For instance, spontaneous wetting, in which there are no constraints in the contact between a fluid and a liquid, is practically different from the forced wetting (*e.g.* a container filled with water); moreover, when considering a rough surface, the intrinsic chemistry of the solid is not enough to describe completely its wetting, since an important role is also played by the roughness of the solid.

1.2.3 Wetting of smooth surfaces

The three interfacial tensions described in the previous paragraph are the only factors that influence the wetting of an ideal solid surface (intended as a smooth, insoluble and chemically homogeneous surface). If the dimension of the liquid drop or gas bubble is of the order of micrometres, these tensions are not influenced by the drop (bubble) size, thus the intrinsic chemistry of each of the phases involved in this phenomenon is reflected by the wetting of a smooth surface.

The grade of a solid surface's wettability is estimated by the contact angle (CA) a liquid droplet (water in our case) produces with it.

In other words, the CA is the angle between the tangent to the drop at the triple line (also

known as the three-phase contact line) and the solid surface. The subsequent equation, known as the Young equation, gives the CA for liquids on straight surfaces in air:

$$cos\theta_Y = \frac{\gamma_{SA} - \gamma_{SL}}{\gamma} \tag{1.9}$$

where θ_Y is the Young CA, γ_{SL} the solid-liquid interfacial tension, while γ and γ_{SA} are the surface tensions of the liquid and solid with gas, respectively.

By analyzing this equation, a positive sign of the cosine implies a $\theta_Y < 90°$, thus a higher value of γ_{SA} with respect to γ_{SL}, a situation typical of the hydrophilic surfaces, in which water tends to cover them.

Viceversa, if $\theta_Y > 90°$ the solid surface repels the liquid and tries to be more in contact with air, behaving in a hydrophobic manner.

A different situation, called CA hysteresis, is taken into account when a smooth surface with a chemically heterogeneous structure is considered. A range of metastable CAs is identified, within which the most thermodynamically stable CA can be computed through the so-called Cassie equation:

$$cos\theta_C = \sum_i x_i cos\theta_{Yi} \tag{1.10}$$

where x_i is the area fraction of chemistry i and θ_C stands for the Cassie CA which represents an average contact angle for the solid surface.

In this way, the wettability of a chemically heterogeneous surface can be studied by using the same terms described for ideal surfaces.

According to the liquid used, which usually has a lower surface tension with respect to water, a smooth surface will show a Young CA different and generally lower than the one for water.

Therefore, the new term "hygrophilic" can be employed to describe this general case although, since no smooth hygrophobic surfaces have been found yet, the fact that a solid surface is hydrophobic does not imply that it is also hygrophobic.

Although a perfect and smooth surface is almost impossible to find in a real environment, a slightly rough surface may be tought to behave as an ideal one in terms of stable CA. Therefore, the study of these two CA is pertinent both to the measurement of a solid surface wettability and to the comprehension of wetting methods on real surfaces as well.

1.2.4 Wetting of rough surfaces

Wetting concerning rough surfaces occurs in two ways: homogeneous wetting (the liquid fills in the grooves of the rough solid thoroughly) or heterogeneous wetting (air is trapped between the liquid and the grooves) [2].

The equation that computes the most stable CA is the following one given by Wenzel, with the assumption of a homogeneous regime and a very large drop in comparison to surface roughness, since when the dimension becomes large enough, gravity dominates and distorts the CA:

$$cos\theta_W = r cos\theta_Y \tag{1.11}$$

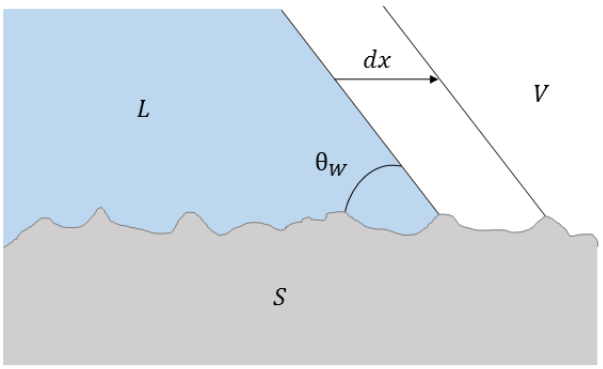

Figure 7: Wenzel state approximation

where r stands for the ratio between the real area of the solid surface to its projection and it is called roughness ratio; thus, it is equal to 1 if the surface is smooth.

The Wenzel equation foresees that the CA value is smaller for a hydrophilic solid surface with instrinsic roughness than the one achieved for a smooth surface ($\theta_W < \theta_Y$) since, as we said before, the latter depends only on the instrinsic chemistry of the three phases.

Viceversa, very high CAs are achieved when a rough hydrophobic surface is taken into account ($\theta_W > \theta_Y$), by taking wettability beyond the threshold values determined by the surface chemistry. It is in fact known that the highest CA value for a smooth surface onto which a water drop is placed is roughly 120° [4].

The assumption made by Wenzel is based on a movement of the drop whose contact line progresses until a final equilibrium configuration, described by the angle θ_W, is reached, and on the fact that the contact line advances following the material asperities, in order to replace each groove of the solid in contact with air with a solid/liquid interface (Figure 7).
The contact line apparent displacement dx leads to a consequent variation in the surface energy per unit length, given by:

$$dE = r(\gamma_{SL} - \gamma_{SA})dx + \gamma dx cos\theta_W \tag{1.12}$$

where the roughness ratio clearly increases the solid surface tensions and thus the corresponding energies.
For a flat solid ($r = 1$), the solution of Equation 1.12 gives Equation 1.8, while Equation 1.11 is satisfied when $r \neq 1$.

Although this behavior is generally observed, the Wenzel assumptions are not always fulfilled. For instance, since the liquid tends to conform to the roughness, it may let the drop to be pinned along the defects, making it difficult to compute θ_W.

However, during the last part of the 1990s, a group of Japanese researchers tried to study the Wenzel behavior of drops by comparing the contact angles achieved on flat surfaces with the ones on rough samples, using different types of liquids [5, 6].

In the hydrophilic domain, they discovered a linear behavior for which, under a limit Young CA value, the apparent CA moves toward 0° when θ_Y tends to zero as well (even if rough, a wettable solid keeps the same properties), a regime due to the so-called hemiwicking, for which

the fluid fills in the grooves created by the asperities of the solid, which in turn lowers its surface energy to accomodate it. The microtexture is thus composed by a liquid/solid mixture onto which the drop is placed, in contrast to the Wenzel hyphothesis, which leads to the definition of a new regime named *superhydrophilic* regime. On the hydrophobic side, they noticed that CAs on flat solids never reached values higher than 120°, which corresponds to the maximum limit achievable for the hydrophobicity due to chemistry only.

Nevertheless, when the roughness domain was exploited, they were able to evaluate contact angles of 170°, which could not be obtained without changing the asperity of the surface, thus leading to the definition of a *superhydrophobic* state for this kind of materials, provided that the solid is coarse enough.

Again, Wenzel assumptions are no longer satisfied since air pockets tend to establish underneath the liquid, a condition also known as Cassie/Baxter (CB) state, which shows very high CAs (larger than 150°) since the drop will sit on a contact area which is mostly occupied by air (which is by definition hydrophobic) and for a small part by the solid-liquid contact. This air surface is uniform and smooth, thus very low hysteresis, which is usually due to chemical heterogeneity and roughness, is present in this wetting regime.

According to this, each liquid droplet may be taken away from any homogeneous surface thanks to its low hysteresis, with no regards to the CA value, even though surfaces with a low contact angle are more prone to losing their chemical homogeneity because of the interplay with the environment.

TABLE II: TERMINOLOGY FOR WETTABILITY CLASSIFICATION

Surface type	Contact angle (deg)
Superhydrophilic	$\theta \sim 0°$
Hydrophilic	$0° < \theta < 90°$
Hydrophobic	$90° < \theta < 150°$
Superhydrophobic	$\theta > 150°$ (low hysteresis)

1.2.4.1 Contact angle hysteresis

When considering the micrometric scale, most of the solids are generally rough and usually fabrication techniques such as lamination tend to increase the presence of microgrooves and striations. Even coating can induce roughness and it will be seen in the experiments later that a thin layer of TiO_2 (in our case) can make the surface of a steel sample, which is by nature hydrophilic (hygrophilic), superhydrophobic (and also oleophobic).

According to Gibbs (1839 - 1903) a contact line can be pinned by the defects a certain solid contains, whether they are chemical heterogeneities or roughness. Whereby, droplets on an incline remain in a relaxation state, producing an asymmetry in contact angles which leads to the formation of a Laplace pressure difference between the rear of small curvature and the front of higher one and thus, provided that the dimension of the drop does not exceed a size limit value, a force able to contrast gravity.

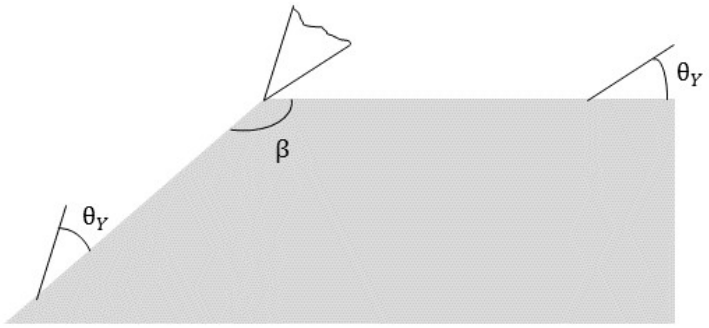

Figure 8: Contact line pinning on the edges of the defect

The edge of a defect, characterized by an angle β, leads to a change in the contact angle at that place, even if a solid with a chemically homogeneous surface is considered. By setting the horizontal as a reference, it is possible to measure a Young CA $= \pi - \beta + \theta_Y$ after the edge and a Young CA $= \theta_Y$ before the edge, two limits which define a range where any angle value can be observed and highlight that grooves can thus prevent the front of a drop to keep spreading, while tips have the opposite behavior so that a solid with this type of flaws causes large and small CAs.

In general, the liquid deposition process influences the value of the CA, thus if a drop slowly deposited is surrounded by nonwetting imperfections, it usually spreads and stops as soon as it

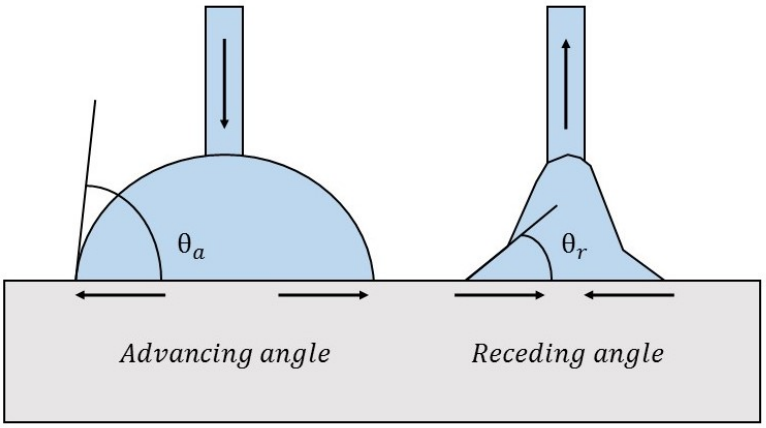

Figure 9: Advancing and receding contact angle

moves toward them, with no possibility for it to explore the solid further.

When the drop evaporates, its configuration is the same as a drop pinned on wetting defects.

A method used for the estimation of the CA hysteresis consists of a very slow increase of the volume of the drop, causing the contact line to suddenly move by overcoming a critical volume of the droplet, after it remained stuck in the beginning, progressing towards a successive series of pinning defects.

The maximum angle observed is what is usually called advancing contact angle θ_a. On the other hand, if the liquid is sucked away from the surface, the drop tends to be flattened until it depins

and moves backwards and the receding CA θ_r is the minimum angle measured (Figure 9). The CA hysteresis is then given by the difference between the two angles:

$$\Delta\theta = \theta_a - \theta_r \tag{1.13}$$

Contact angle hysteresis may be harmful (e.g. water drops that remain stuck on glass panels augment degradation by changing their transparency) but also beneficial (e.g. when utilized for guiding a flow along a series of defects, following a stable itinerary).

1.2.5 The capillary length

Among the most important characteristics of a liquid is their capacity to defeat gravity and build capillary bridges, rise on inclined planes or in small capillary ducts, even though liquids can change their spherical shape when subjected to the gravity force.

The parameter that dictates the importance of gravity is called *capillary length*, expressed as κ^{-1}, whose value is assessed by a comparison between the hydrostatic pressure and the Laplace pressure, evaluated in a liquid characterized by a density ρ which undergoes the effect of earth's gravity $g = 9.81\ m/s^2$.

Equalizing the pressures γ/κ^{-1} and $\rho g\kappa^{-1}$ we achieve:

$$\kappa^{-1} = \sqrt{\gamma/\rho g} \tag{1.14}$$

where κ^{-1} is usually of the order of mm and can be increased by either operating in microgravity or substituting air with another liquid having a lower density.

If the largest dimension of the drop, here called r, is lower than κ^{-1}, the effect of gravity is negligible and the capillary effects dominate.

Viceversa, for $r > \kappa^{-1}$, we find the system to be in the gravity regime.

CHAPTER 2

FLUID TRANSPORT

The transport of a liquid drop on an open substrate, driven solely by the capillary force and without the need of other devices, has gained great importance in the last years, especially in the biomedical field for the fabrication of diagnostic devices.

Handling a small volume of liquid on these substrates can reduce the friction among the channel walls and the fluid, removing in this way the possibility of air-bubble clogging and minimizing the contamination between samples.

However, some aspects must be taken into account and thus improved in order to better perform this kind of task, such as the control of the dispensed liquid and a rapid pumpless transport. Thermocapillarity, gravity and magnetic force are just three of the most common forces considered in order to achieve microfluidic liquid transport.

Groups of researchers have shown that passive transport can be achieved by altering the chemical pattern of surfaces, as well as their physical texture, obtaining a surface tension driven phenomenon when drops get placed on wedge-shaped hydrophilic tracks surrounded by a hydrophobic substrate.

A study regarding low-cost microfluidic transport has been conducted by Ghosh et al. [7], who created a substrate-independent method to guide small volumes of liquid on superhydrophilic diverging tracks by overtaking opposing and viscous forces and achieving high velocities and micro flow rates.

The droplet, which is significantly larger than the track width, is deposited on the track's narrow side and thus constricted by the boundaries along the transverse direction and free to spread toward the wider region. The initial propagation of the film is due to hemiwicking through the roughness of the substrate, but this is also heavily affected by the Laplace pressure difference throughout the track length, leading the initial liquid bulge to gradually adopt a rivulet like shape along the wedge path.

This behavior was previously noticed by other researchers, who demonstrated that a liquid flowing on rectangular tracks acquires a shape proportional to its volume and inversely proportional to the cube of the track width (V/w^3).

A semi-cylindrical shape is assumed by the liquid, provided that this ratio does not reach a threshold value depending on both the equilibrium CAs on the superhydrophilic and superhydrophobic domains.

As a first result, it has been seen that the liquid is prone to moving forward, towards the wider side of the track, causing a reduction in the surface energy along that direction. Furthermore, surface tension forces act on both the trailing and leading boundaries of the water and over the pinned sidelines.

Lastly, the liquid touching the sidelines shows a CA higher than 90°, as seen in Figure 10. Globally, the net component of this force is directed to the wider region, propelling the drop towards it, a behavior not seen when straight tracks are considered.

By varying the wedge angle and the track width, it is thus possible to increase or reduce the net capillary force or, more properly, the Laplace pressure gradient, which is actually the reason

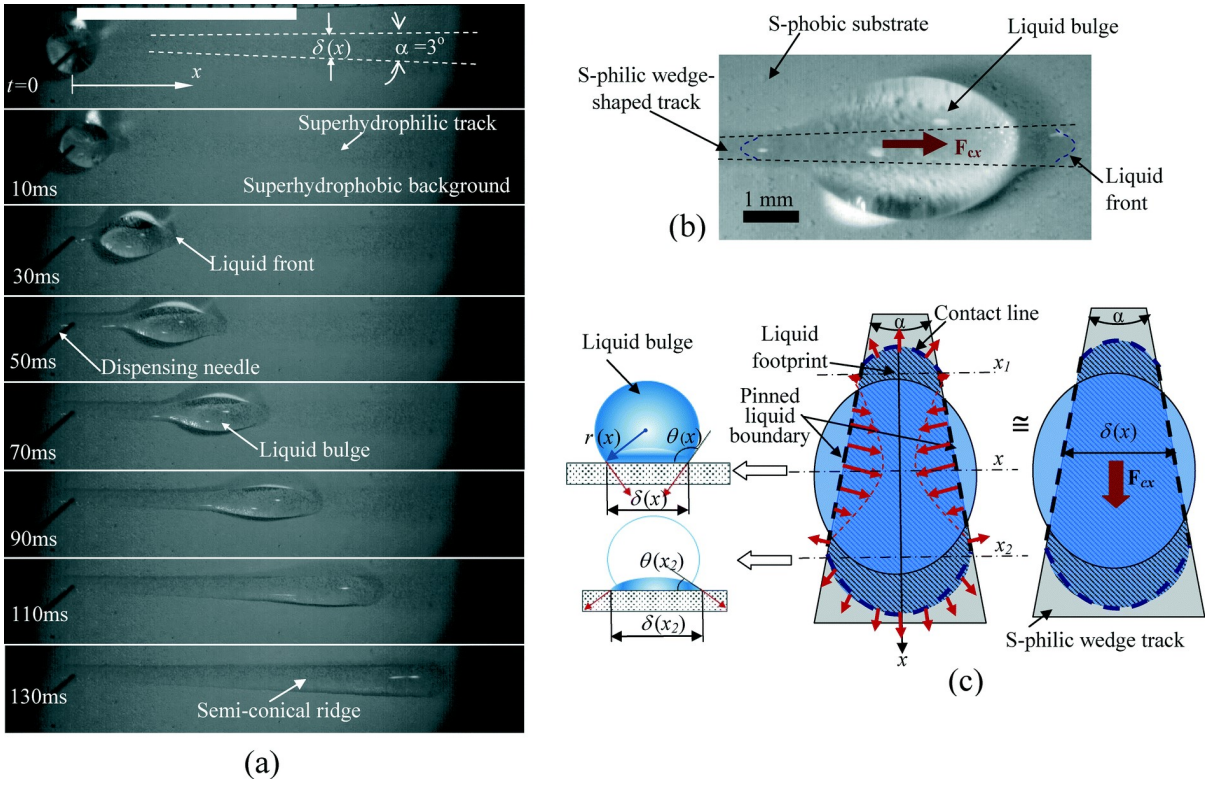

Figure 10: Liquid transport on a diverging track [7]. (a) Time-lapsed images (top view) of liquid transport through the wedge-shaped superhydrophilic track on a horizontal Al-substrate. The white bar at the top denotes 10 mm. (b) Morphology of the liquid bulge, approximated as an ellipsoid of finite footprint on the wedge-shaped superhydrophilic track, moving along the track; (c) origin of the driving capillary force on the liquid bulge.

why this kind of microfluidic transport is possible when superhydrophilic tracks are employed without the need of external power supplies.

By calling $\gamma/r(x)$ the Laplace pressure of the liquid drop at a given section and $r(x) \approx w(x)/[2sin\theta(x)]$ its local curvature, it is possible to compute this pressure gradient, after having assumed an average value of θ_{avg} along the bulge length:

$$\frac{dP}{dx} \sim -\frac{d}{dx}\left[\frac{\gamma}{r(x)}\right] \sim -\gamma\frac{d}{dw(x)}\left[\frac{2sin\theta(x)}{w(x)}\right]\frac{dw(x)}{dx} \sim 2\gamma sin\theta_{avg}\frac{1}{w(x)^2}\alpha \tag{2.1}$$

where α stands for the wedge angle [7].

CHAPTER 3

THERMOCAPILLARITY

3.1 Introduction

As previously discussed, the surface tension represents one of the most outstanding localized properties regarding the interface between two different immiscible fluids. The characteristics of γ can be highly influenced by the presence of external materials on the interface, as well as by other physical factors which, according to what is here presented, have a more interesting aspect from the engineering point of view.

According to the studies made by Levich (1948), scalar quantities such as the temperature and the electrical field contribute to modify the features of the surface tension, the first one having gained great importance in the recent years.

The purpose of this section is thus to give a quick overview of the most common types of thermocapillary instabilities, which are based on this initial equation of state:

$$\gamma = \gamma(T) \tag{3.1}$$

The following linear equation shows the dependence of γ on temperature:

$$\gamma = \gamma_0 - m(T - T_0) \tag{3.2}$$

In addition, Σ denotes the interface between the fluids.

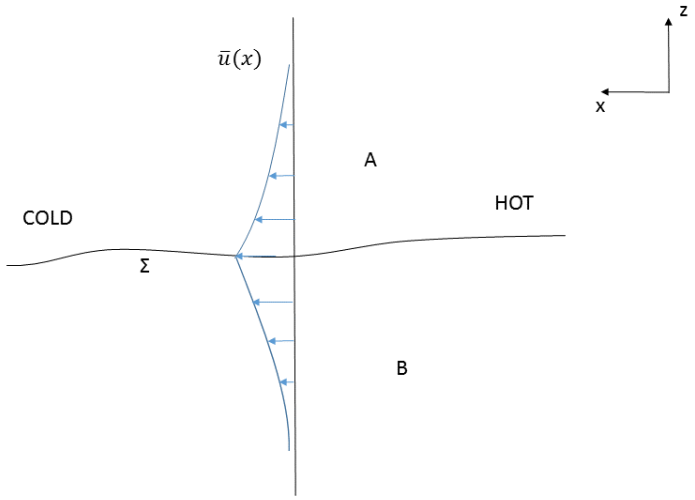

Figure 11: Forced temperature gradient along the interface between two non-miscible fluids

Figure 11 shows an interface between fluid A and B along which the enforcement of a temperature gradient induces a subsequent spatial gradient in surface tension, the latter balanced by shear stresses at the interface which arise as a consequence.

The value of m for ordinary liquid is usually lower than zero ($m = -\frac{d\gamma}{dT} > 0$), meaning that the fluid tends to move from the hot to the cold side. Due to their viscosity, fluids are dragged along and the temperature gradients at the interface Σ are responsible for this motion.

Levich found in this behavior the so-called *thermocapillary effect.*

This phenomenon is the basis of the flame propagation over liquid fuels, the breakage of thin films and the contact line movement, as well other important behaviors related to the heat transfer.

In many occasions, additional processes can augment the heat transfer rate across an interface throughout the presence of some instabilities and clearly, those driven by thermocapillarity can affect the surface tension and the properties of that specific interface.

3.2 Experimental background

Many researchers have tried to study the thermocapillary effect on different types of substrates, using a various range of oils as a primary liquid and running many distinct experiments.

One of the first papers ever published and currently hidden from scientific attention was written by A. I. Fedosov (1923 - 1999), who based his study on the introduction of a mathematical description of the thermocapillary effect, treating the movement of a flat liquid layer [9].

A nonuniformly heated liquid experiences convection due to the dependence of density on temperature and, when an interface is present in it, the thermocapillary motion also appears [9].

A flat container with a depth sufficiently smaller than its width and length is considered, which leads to neglecting the convective flow. The direction parallel to the container length is considered to be the x axis, along which a constant temperature gradient is applied.

Fedosov estimated that for large temperature gradients, the thermocapillary mass flux prevailed

over the convective one, provided that the interfacial heating layer of liquid was sufficiently thin as Birikh detected [10].

A similar investigation has been recently conducted by Barakhovskaia, Marchuk and Fedorets, who have employed two different silicone oils (PMS-5 and PMS-50) to study both analitically and experimentally the thermocapillary deformation's depth in a locally heated horizontal liquid layer, as a function of the layer's thickness [11].

They discovered that for very thin layers, the depth h of the deformation rises, provided that evaporation is neglected and that other parameters such as viscosity, gravity and capillary pressure are taken into account.

Furthermore, when the thickness of the layer is greater than $400\mu m$, the magnitude of the deformation remains constant, since the change in the viscosity has a weaker effect on the distortion, a behavior that is thus in accordance to what Fedosov and Birikh proposed in their works.

It is also worth to mention the work done by Davis (1939), who proposed a one layer system as a simplified case to study the mechanisms of thermocapillary instabilities, composed by a liquid film delimited by a rigid plate in the bottom part and an ideal passive gas in the upper part (Figure 12). [8]

As a basic assumption, the liquid is considered to be a Newtonian fluid whose properties such as density ρ_0, viscosity μ, thermal conductivity k, specific heat c_p and volume expansion coefficient υ are constant, while the kinematic viscosity $\nu = \frac{\mu}{\rho_0}$ and the thermal diffusivity $\kappa = \frac{k}{\rho_0 c_p}$ are also employed.

The gravity force g acts on the system, while Equation 3.2 provides the variation of the surface

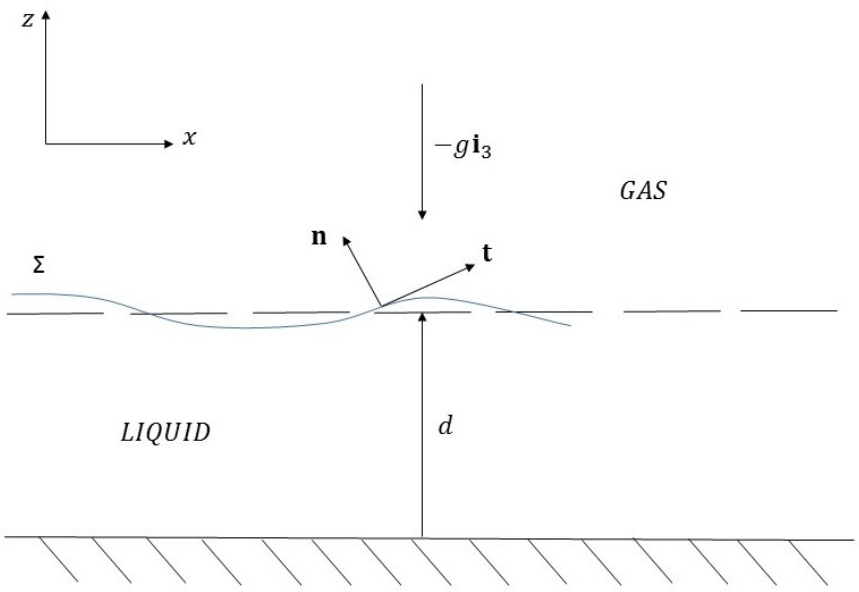

Figure 12: Scheme of a one-layer system

tension γ with respect to the temperature T.

A temperature gradient ∇T is applied to the system with no precise orientation:

$$\nabla T = -a_{\parallel}\mathbf{i}_1 - a_{\perp}\mathbf{i}_3 \tag{3.3}$$

in which $|a_\perp|$ and $|a_\parallel|$ are the magnitudes related to the temperature gradient applied in the normal and parallel direction, $\mathbf{i}_1, \mathbf{i}_2, \mathbf{i}_3$ are the unit vectors along the x, y, z directions, while the module can be defined as $a = \sqrt{a_\parallel^2 + a_\perp^2}$.

Two situations have been taken into account. On one hand, the thermal gradient can be imposed normally to the interface Σ, thus $\mathbf{i}_1 \nabla T = \mathbf{i}_2 \nabla T = 0$ yields to a static base state where the surface tension gradient at the interface is balanced by a shear stress which results in fluid motion [9], a kind of instability which leads to the so-called steady Marangoni convection.

On the other hand, if the temperature gradient is enforced in parallel with Σ, there exist no static states and a shear flow would be driven by thermocapillarity, whose instabilities were identified by Smith and Davis as a kind of time-periodic hydrothermal waves and the bulk seen to be penetrated by the flow at the interface [8].

From Equation 3.3, setting $a_\parallel = 0$ and $a_\perp > 0$, the Marangoni instability is analyzed; viceversa, if $a_\parallel \neq 0$ and $a_\perp = 0$, the hydrothermal waves problem is investigated.

CHAPTER 4

EXPERIMENTAL PROCEDURE

4.1 Overview of the experiments

The set of experiments which will be described in the following paragraphs has the main goal of demonstrating the presence of a temperature dependent behavior of the shape of liquid films resting on wettability-confined tracks, when subjected to a costant spatial temperature gradient imposed on the system.

Furthermore, the consequent change in volume distribution along both straight and wedge-shaped superoleophilic tracks surrounded by an oleophobic structure, which prevents their spreading outside the track itself, has been also investigated.

Subsequently, an experimental analysis has been performed in order to investigate the parameters that affect this process and the repeatability of this kind of procedure, which often can fail to be assessed if the wrong liquids, materials and overall conditions are employed and applied. For example, since the need for very thin liquid films is crucial for this kind of problem, a fluid with a low value of γ is strongly required, thus the avoidance of water, which has a high value of surface tension that can prevent the fully wetting of a surface. Moreover, due to its volatility, water would evaporate soon after the temperature was lifted above the standard ambient value.

Furthermore, the surface tension and the capillary length play a huge role in micro scales (gradients in γ lead to Marangoni stresses), hence a tiny and compacted setup has to be realized by dimensioning everything according to these two parameters.

4.2 Materials and methods

A steel plate (AISI 1018, thermal conductivity of 51.9 $\frac{W}{mK}$, 2.3 mm-thick, 12 mm x 36 mm, McMaster-Carr) is used as a substrate.

The chemicals employed include TiO_2 titanium(IV) dioxide nanoparticles (anatase, <25 nm, 99.7% trace, Sigma Aldrich), fluoroacrylic copolymer dispersion (PMC) manufactured by Dupont (20 wt.% in water; Capstone®ST-100), ethanol ($\sim$ 100 wt.%, Decon Labs) and acetic acid (A38C-212, Fisher Scientific).

The TiO_2 nanoparticles are meant to impart the micro- and nanoscale roughness, whilst the PMC copolymer is used as the primary component of the oleophobic surface. Furthermore, ethanol is used as a solvent in order to disperse the TiO2 particles and the PMC, controlling the solids content and making the formulation more sprayable due to its volatility, while the acetic acid is utilized to lower the pH and make the formulation more stable. The process of preparing such formulation has been followed according to the passages hereafter provided.

First, 0.525 g of TiO_2 was added to 13.15 g of ethanol and probe sonicated (750 W, 13 mm probe diameter, 40% amplitude, 20 kHz frequency, Sonics and Materials Inc., model VCX-750) by enforcing 1000 J of energy, followed by the addition of 1.125 g of PMC solution. Then, 0.2 g of acetic acid was added to complete the dispersion. The final content was manually shaken

at room temperature to form a stable solution and then sprayed on the samples by means of an airbrush (VL-202S siphon feed, 0.73 mm spray nozzle, at 30 psi air pressure, Paasche) in order to impart the oleophobic texture. Moreover, a heat gun was used in between passes to evaporate excess solvent from the substrate, thus achieving a better coating quality at the end. Afterwards, the spray-coated samples were cured on a hot plate at 150°C for 15 minutes, with the aim of assisting the complete coating of the particles by the PMC.

Sessile CA measurement performed showed an average value of 110° ± 2.64° when the 50 cSt oil (PMX-200, Dow Corning Xiameter) was employed.
This liquid was chosen thanks to its low volatility and low surface tension, which keeps it free of surfactant contamination and allows very thin films on smooth surfaces which could not be achieved if a fluid with higher surface tension (e.g. water) were used.

Finally, the oleophobic steel surface was ablated with a Yb:Fibre laser (Wavelength 1060-1080 nm, 20 kHz, 10% power, Tykma Electrox) beam to produce either the straight or the wedge-shaped track, by removing the coating and re-exposing the underlying superoleophilic substrate.

4.3 Analysis of the substrate

All the samples used for the experiments have been weighed before and after the coating procedure, showing an average increase in their weight from which it was possible to measure the average amount of solution sprayed onto them.

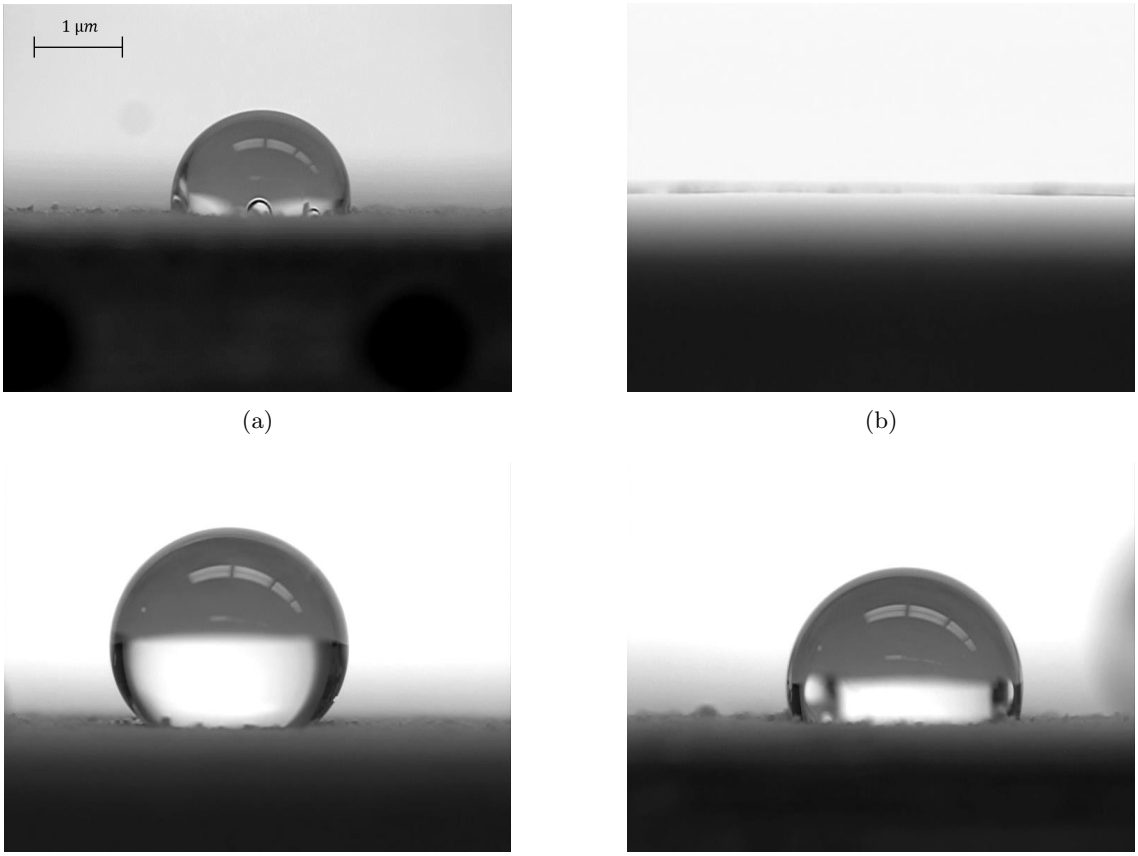

(a) (b)

(c) (d)

Figure 13: Contact angle for different liquid droplets placed on the oleophobic substrate, *a*) Silicone oil on coated substrate, *b*) Silicone oil on uncoated substrate, *c*) Mineral oil, *d*) Hexadecane.

An average value of 16.26 ± 0.43 GSM (grams per square meter) has been obtained.

Contact angle measurements were performed at this time in order to visualize the effective change in the surface behavior from superoleophilic to oleophobic (superhydrophobic), by employing different types of liquids (Figure 13).

First of all, a test with the 50cSt viscous silicone oil utilized for the experiments has been run both on the coated and on the uncoated substrate of the steel samples (13(b) and 13(a)), in order to check the oleophobicity of the coating and show the natural spreading along their uncoated surface, which is intrinsically superoleophilic, respectively.

Furthermore, an additional aim was to visualize the confinment created by the contrast between the two different textures currently present, which serves as a boundary to prevent the spreading of the oil outside the etched track.

In this case, the coated substrate shows an average CA value of 110° ± 2.64° with the silicone oil employed, which confirms the good oleophobicity predicted.

Then, two additional liquids have been tested (Hexadecane and Mineral oil) which showed the CA values given in Table III.

Although these liquids have larger contact angles with the substrate than silicone oil, the latter has been chosen due to its high purity and low volatility, as well as for the large variety of viscosities available, which can be exploited to potentially investigate this effect in the future, and mainly for its extremely low surface tension which keeps it free of surfactant contamination.

TABLE III: CONTACT ANGLE MEASUREMENTS

Liquid	Surface tension (mN/m)	Average contact angle (deg)
Mineral oil	27	125° ± 2.64°
Silicone oil	20.8	110° ± 2.64°
Hexadecane	18.43	114° ± 1.73°

4.4 Experimental setup

The setup designed for the experiments (Figure 14, Figure 15) is composed of three PTFE blocks (McMaster-Carr), one meant to accomodate the electronic devices, the heat sink and the sample, the other two ones to create a compacted structure, through the two fastening nuts and the long screws, in order to minimize the heat losses and provide good thermal contact by compression.

Two Thermoelectric (Peltier) micro modules (TE-65-0.6-0.8, TE Technology Inc), 2.55 mm-thick, 13 mm x 12 mm, able to operate in the temperature range -20° ÷ +80°, are employed: the first one aims at supplying heat to the left hand side of the steel sample, the second one cools down the right hand side.

Each of the two Peltier stages is kept in touch with the sample by means of a thin layer of thermal paste (OMEGATHERM® 201) which has the additional function of helping the thermal conduction between the two surfaces. A copper plate, protruding from the front face of the setup (2 mm-thick, 13 mm x 38.1 mm, McMaster-Carr), is used as a heat sink to cool down the hot side of the cooling micro module, being compacted in between two copper blocks

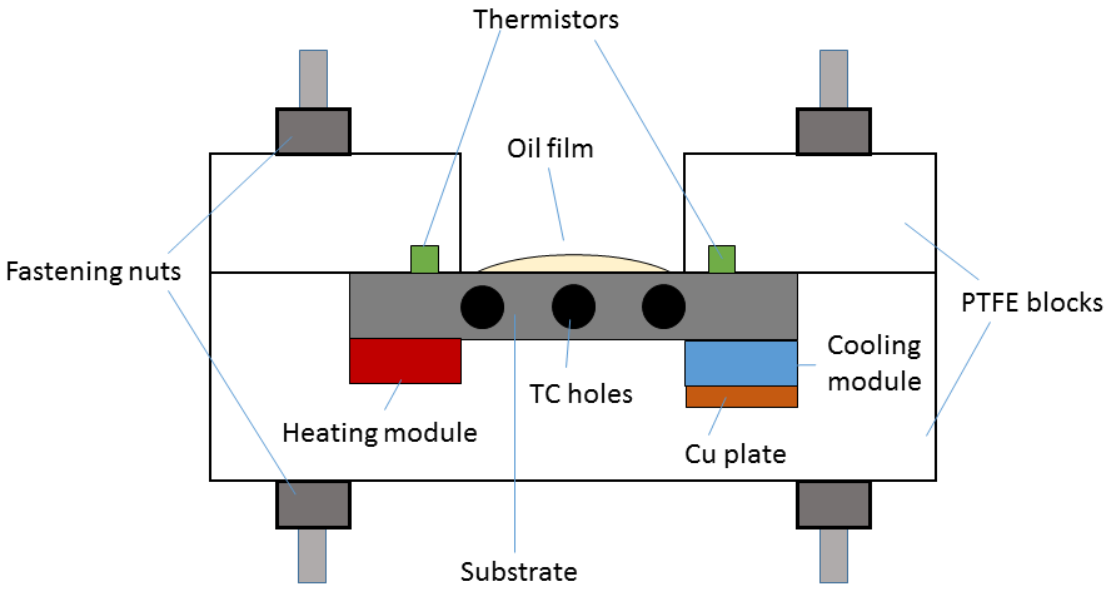

Figure 14: Side view of the setup

through which water from a container with melting ice was circulated, simulating a cold plate arrangement.

Two bi-polar proportional-integral-derivative (PID) temperature controllers (TC-36-25-RS232, TE Technology Inc) are utilized to monitor the temperature of the Peltier modules. Since the maximum allowable voltage for these modules is 9.6 V, a two-power supply configuration is performed: one power supply (PS-24-6.5, TE Technology Inc), ranging anywhere from 12 to

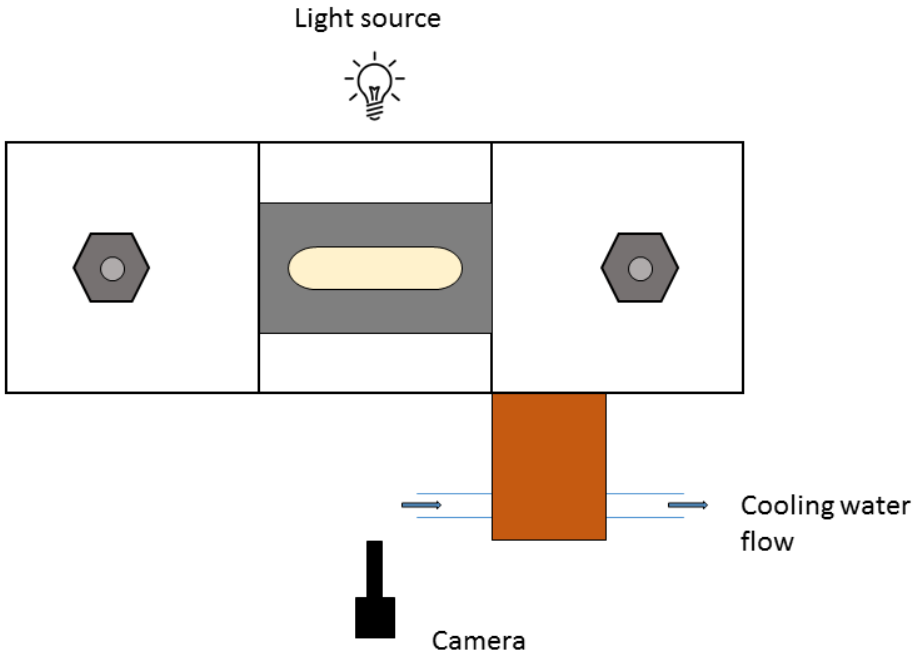

Figure 15: Top view of the setup

36 VDC, can be used to power the controller itself; a second power supply (PS-24-6.5, TE Technology Inc), ranging anywhere from 0 to 36 VDC, can be connected to the H-bridge of the controller.

The electrical H bridge configuration is realized to automatically control the direction of current according to the temperature set point. This second power supply allows the controller to monitor the TE devices that must operate at a voltage less than 12 V.

The controller is programmable via the RS232 communication port for direct interface with a compatible computer. The software provides a graphical user interface for setting control parameters and receiving feedback from the temperature sensor.
Two types of control output modes may be selected to determine the direction of the current flow through the thermoelectric when heating is desired.

Two thermistors (MP-3193, TE Technology Inc) are used with the temperature controllers for a temperature feedback/control of the hot and cold side of the steel plate, both being kept in contact with the latter by a thin layer of thermal paste.
Six K-type thermocouples (Omega, bead diameter 0.13 mm) are used for the temperature measurement at relevant locations on the sample and positioned along the longitudinal direction of the track.

Three thermocouple holes are drilled into the plate at a depth of 6 mm in order for the TCs to reach the centrally-placed track at its initial, central and final point, while the other three holes are positioned on the other side of the steel sample at a depth of 3 mm, in order to record the temperature value at that specific point and compare it to the one measured by the previously mentioned thermocouples, with the aim of evaluating the temperature gradient along the transversal direction of the track (Figure 16). Temperature data are registered with a differential data acquisition system (Omega DAQ USB 2400 series) at a sampling frequency of 1 Hz.

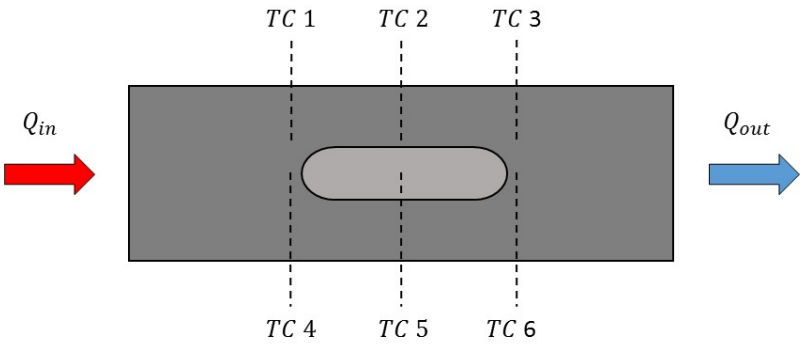

Figure 16: Top view of an etched steel sample with a straight track and thermocouple holes positioned along the length of the plate

4.5 Preliminary procedure

The first preliminary experiment was conducted to evaluate the thermal response of the Peltier micro modules and to record the temperature values measured by the six thermocouples, with the aim of determining the temperature difference along the longitudinal and the transverse directions of the steel plate.

The final goal of this procedure consists of supporting the hypothesis of a one-dimensional system, based on two main assumptions which neglect both the temperature gradient along the oil film thickness (z direction) and along the transverse direction (y direction) of the track.

Therefore, the one-dimensional form of the Fourier's law is hereafter considered:

$$Q = -kA\frac{dT}{dx} \tag{4.1}$$

where Q is the heat flux provided to the steel sample through the hot Peltier module, which is then taken away from the cold module, $k = 51.9\frac{W}{m \cdot K}$ is the thermal conductivity of the AISI 1018 steel plate, $A = 27.6mm^2$ is the cross-sectional surface area and $\frac{dT}{dx}$ is the temperature gradient along the longitudinal direction of the sample.

The first assumption, based on the neglection of the thermal gradient along the vertical direction of the oil film, can be validated through the analysis of the Biot number, which characterizes the heat transfer resistance within a body and equivalently expressed as the ratio between its surface conductance and its internal conduction:

$$Bi = \frac{Lh}{k} \tag{4.2}$$

where h is the heat transfer coefficient, roughly $\sim 7.5\ \frac{W}{m^2K}$ in the case of natural convection, L is the characteristic length, equal in this case to a maximum film thickness value of $\sim 350\ \mu m$, and k is the silicone oil thermal conductivity, equal to $0.14\ \frac{W}{mK}$.

Substituting these values in the equation, a $Bi \sim 0.0187 << 0.1$ is obtained, indicating that the conduction in the body is much faster than the heat convection away from the surface and leading to the neglection of the vertical temperature variation within the liquid film,

which in turns allows to consider the temperature of the air-oil interface equal to the substrate temperature.

Furthermore, the choice of very thin film thickness, a condition for which the thermocapillary flow overcomes the convective flow as explained by Fedosov [9], permits a better visualization of this phenomenon in terms of liquid movement toward the cold side of the plate.

The validation of the second assumption goes through the analysis of the results obtained by testing an uncoated steel sample, shown in Figure 17.

In order to be able to study the thermocapillary effect on the fluid in the most effective way,

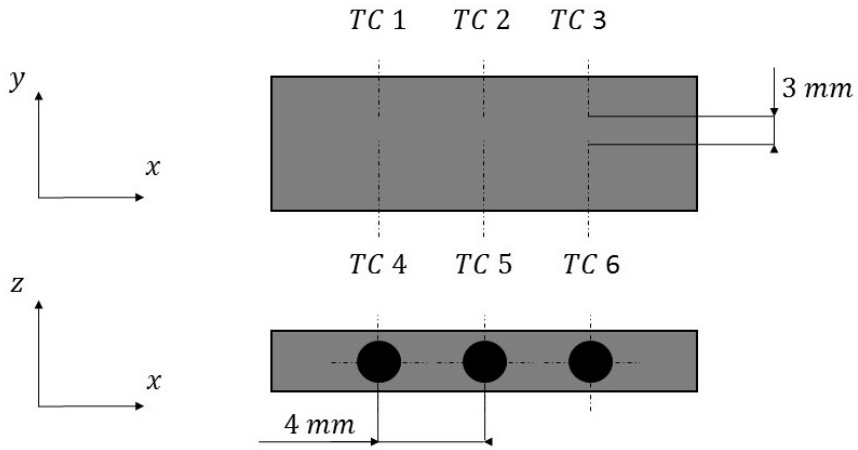

Figure 17: Distances between thermocouples embedded in the sample

it has been decided to let the heating micro module work at half of its maximum allowable temperature first, thus setting a temperature value of $45°C$ for the hot side, and then to increase it up to $80°C$, which corresponds to the upper admissible threshold.
The two Peltier modules being equal and knowing that they are more effective in the heating phase rather than in the cooling one, it has been decided to utilize the cooling module always at its maximum capability, thus stabilizing the temperature according to the maximum value reached by the heating one.

By looking specifically at these two cases, when the steady state is reached, the graphs (Figure 18 and Figure 19) show a constant temperature difference between each thermocouple placed along the longitudinal direction on both sides of the sample.
Moreover, looking at the measurements performed by all six thermocouples, within the limits of error, it is possible to ascertain a similar behavior along the y direction.
Multiple steps, corresponding to a increase of the Peltier temperature by $5°C$ each, are shown in order to fully exploit the performance of the system.

Knowing the distance between each thermocouple seat (Figure 17), it has been possible to compute the maximum temperature gradient along the transverse direction of the sample by specifically looking at the temperature reading of the two thermocouples close to the hot side of the plate (TC1 and TC4), which have the highest difference in temperature (Figure 19).
Values of $\frac{dT}{dx} = 2.25\frac{°C}{mm}$ and $\frac{dT}{dy} = 0.7\frac{°C}{mm}$ are obtained respectively, the latter deriving from the maximum temperature difference observed in this direction ($\sim 2°C$) which can be considered to be within the thermocouple error limits ($\pm 1.1°C$).

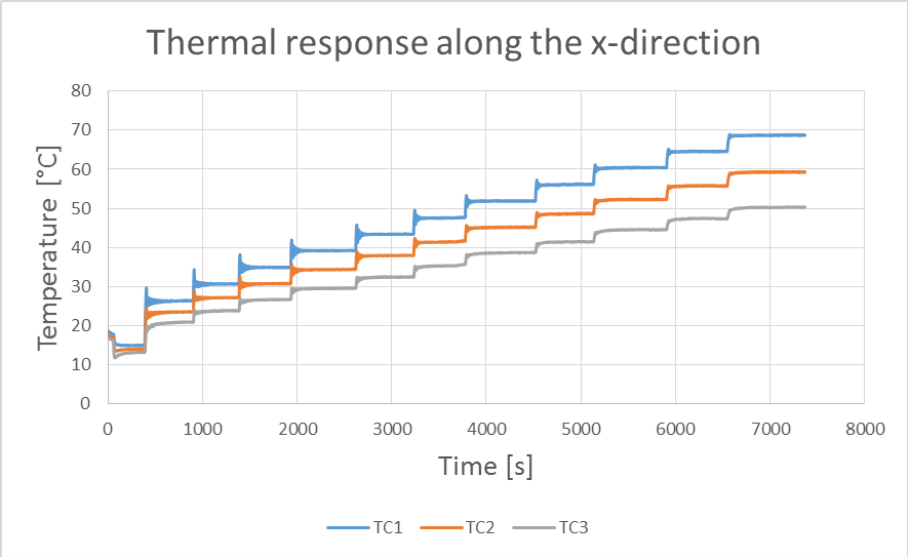

(a)

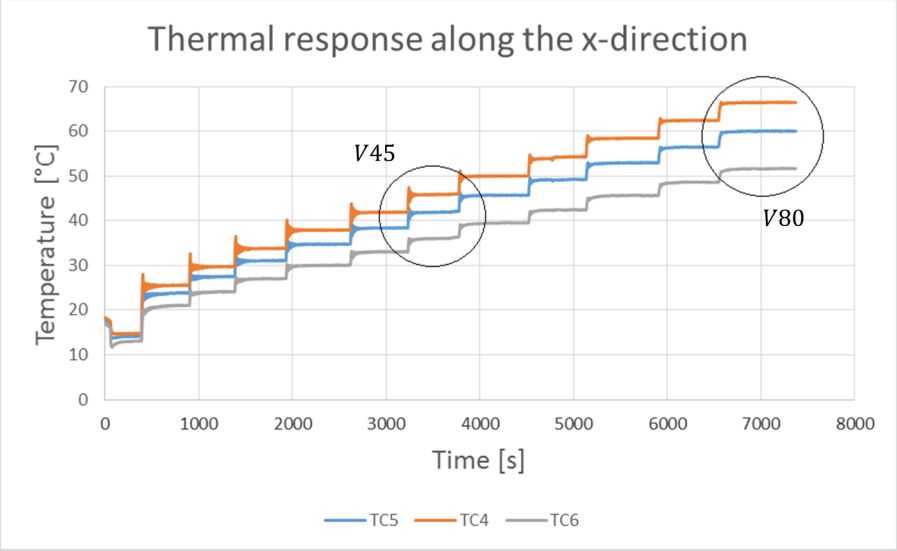

(b)

Figure 18: Temperature differences between the thermocouples on the front and back side of the sample, *a*) Camera side, *b*) Back side.

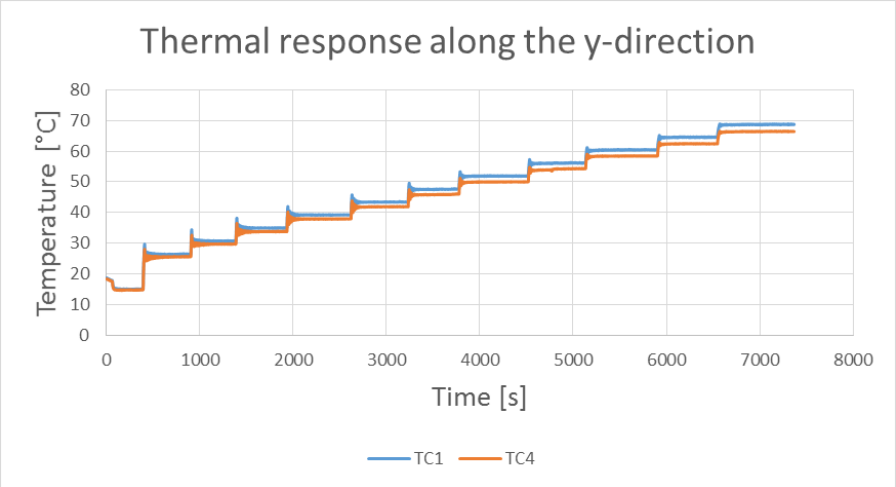

Figure 19: Temperature differences between the thermocouples along the transverse direction of the sample

In addition, the Marangoni stresses in this direction will be acting on the film from the center towards the edges of the track on opposite directions, thus not changing significantly its shape.

For the above reasons, this temperature gradient has not been considered and all the temperature measurement along the longitudinal direction of the plate have been effectuated by means of the thermocouples placed right below the track, which also give a more accurate result.

4.6 Experimental procedure

The lower part of the setup needed for the experiments is fixed to an adjustable (x,y) stage by means of two long screws and leveled according to the height of the focal point of the lens

(Telecentric zoom lens, Navitar) used to capture images of the oil film and attached to a camera (Mintron HD1080p).

A thin layer of thermal paste ($\sim$ 100 μm) is applied both on the thermistors and on the surface of the two micro modules to create a good thermal adhesion between these and the steel sample; then the setup is assembled and compressed using the fasting nuts to ensure proper thermal contact which minimizes contact resistance losses and increases the reliability and repeatability of the experiments. The samples onto which a wedge-shaped track is etched are strategically positioned with the diverging part close to the hot Peltier module, in order to investigate the interplay between the Marangoni stresses and the capillary force created by the diverging tracks.

The characteristic features of each track are shown in Table IV.

The radii of both the narrow and wide end of the track have been chosen after having computed

TABLE IV: TRACK SPECIFICATIONS

Track type	Track angle (deg)	Length (mm)	Width of the narrow end (mm)	Width of the wide end (mm)	Area (mm^2)
Wedge-shaped	2°	7	1.26	1.48	9.19
	4°	7	1.04	1.48	8.50
	6°	7	0.82	1.48	7.83
Straight	-	7	1.48	1.48	9.89
	-	6.52	1.48	1.48	9.19
	-	6.06	1.48	1.48	8.50
	-	5.61	1.48	1.48	7.83

the value of the capillary length for the oil here employed ($\kappa^{-1} = 1.48mm$) and thus dimensioned according to the number obtained, as it will be explained more in detail in the next paragraph. The three thermocouples are then placed inside their seats, after being covered by thermal paste to promote the contact with the sample.

The dispensing of the silicone oil is accomplished by means of a micro pipette (0.5 - 10 μL capacity, Eppendorf Xplorer) fixed to a vertical rod and free to move along the vertical direction (Figure 20).

A total volume of 1.5 μL was initially thought to be dispensed in three equal steps of 0.5 μL each, waiting for the oil to spread uniformly along the track between every deposition interval. However, due to the employment of non oleophobic tips, some reminiscent oil was found outside the tip walls, thus preventing the liquid to be fully deposited on the track.

Furthermore, the presence of air inside the tip, a consequence of the aspiration of oil from its container, reduced the precision during the dispensing phase, thus diminishing the amount of oil placed on the samples.

Once the oil has been completely deposited, four different pictures are taken with the camera by zooming toward the track at four different consecutive points, aided by a ruler strategically placed in between the two PTFE upper blocks, which serves as a physical reference to visualize the starting and ending point of the track itself in each picture.

Furthermore, this way of picturing the film in split zoomed in photos was chosen to minimize the pixel size in relation to the film size, thus minimizing errors related to image processing of the results.

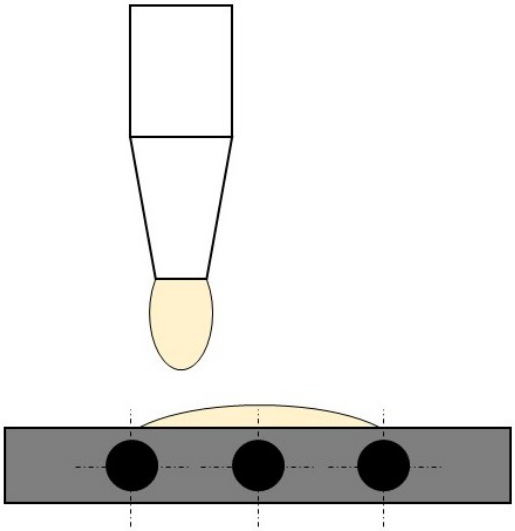

Figure 20: Schematic of the deposition of oil on the substrate

The first photos depict the oil film in the isothermal case, which is the first of three different thermal states analyzed during the experiments.

The power supply connected to the cold micro module is then turned on at a voltage of 9.1V in order to start the cooling process of the steel sample.

It is important to remember that the temperature measurements used to describe the thermo-capillary effect are based on the thermocouple readings and not the Peltier temperatures, the latter only used to stabilize the system at a certain steady state.

Moreover, even though the modules are set at the same temperatures, a different temperature gradient is found for some of the cases analyzed, due to differences in ambient conditions.

After the system has reached the steady state, the second power supply connected to the Peltier module (meant to heat the steel up) is activated at a voltage of 5V, thus increasing the temperature up to the set value of $45°C$; the second series of images is here taken in order to capture the displacement of the oil film toward the cold side.

A subsequent change in the temperature setting value at $80°C$ leads to the third thermal state, during which the thermocapillary effect is most evident and thus recorded once again by the camera. Lastly, the power supply connected to the hot micro module is turned off in order to decrease the temperature of the sample down to the initial ambient temperature value, thus allowing capture of the last four pictures.

The last set of images is taken once again at the isothermal state to ensure that the film reverts back to its original shape after the Marangoni stresses disappear.

CHAPTER 5

RESULTS AND DISCUSSION

5.1 Water behavior on wedge-shaped tracks

The following analysis has been conducted with the aim of explaining the behavior of fluids when placed on wedge-shaped tracks in isothermal conditions, for which the Laplace pressure difference and, in most of the cases the gravity force, play an important role for the understanding of the physics which rules this particular phenomenon.

Specifically, when placing a fluid on a wettability-confined track, minimization of its surface energy forces it to acquire the shape shown in Figure 21(a).
Clearly, the larger accumulation of liquid at the wider end of the track is a consequence of this mechanism. However, when the length of the track is larger than the capillary length, gravity starts to slightly distort the shape of the liquid pushing some of it towards the narrow end. As a result, the curvature of the film changes in a way that the Laplace pressure is higher at the narrow end of the track to balance the effect of gravity, leading to a Laplace pressure difference along the length of the track.

This preliminary study has been performed by employing a 6 mm and a 8 mm long track with a wedge angle of 6°, onto which a specific amount of volume of water has been deposited in order to achieve a very similar maximum film thickness on both of them.

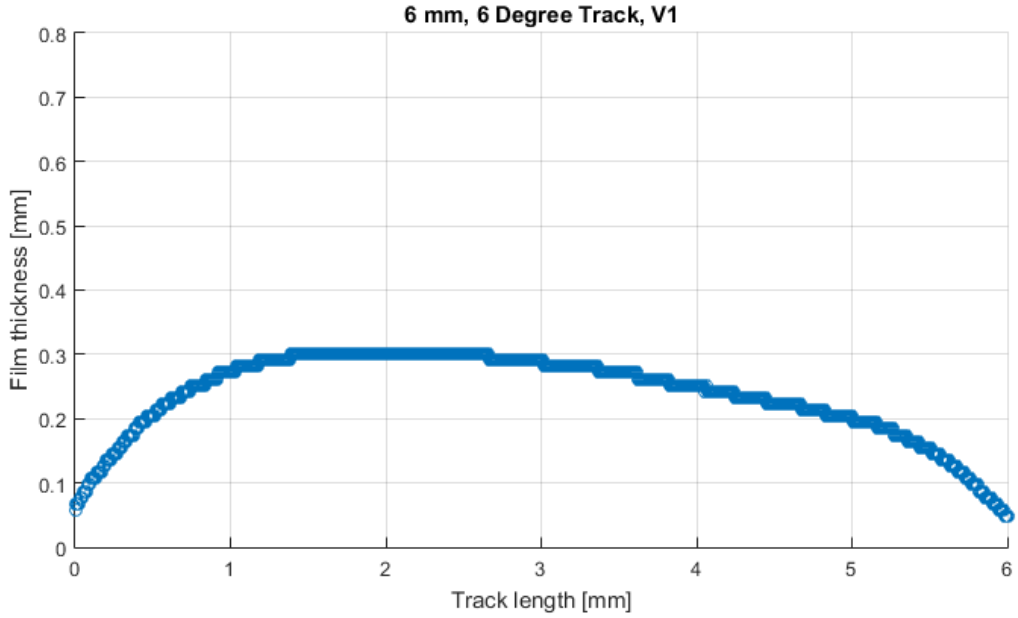

(a)

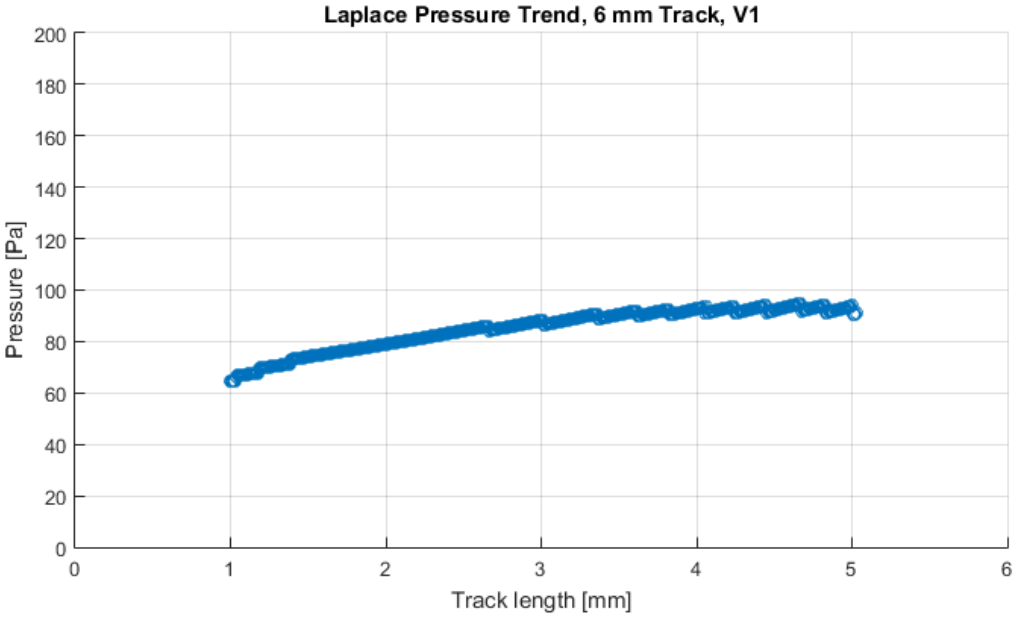

(b)

Figure 21: Water film thickness distribution (a) and Laplace pressure variation (b) for a wedge-shaped 6 mm long track, low volume case. The narrow end of the track is on the right.

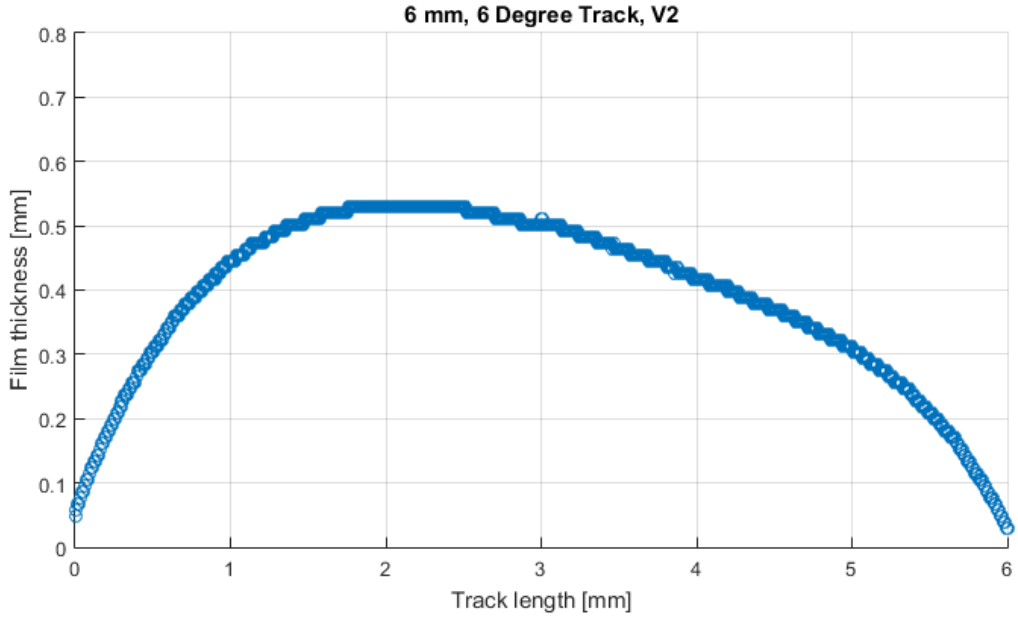

(a)

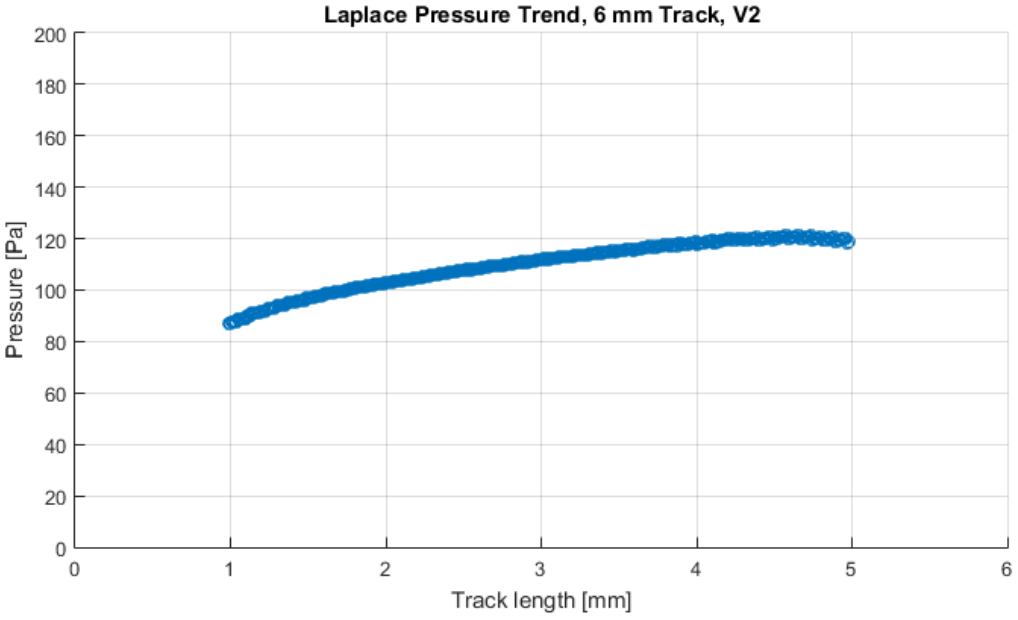

(b)

Figure 22: Water film thickness distribution (a) and Laplace pressure variation (b) for a wedge-shaped 6 mm long track, high volume case. The narrow end of the track is on the right.

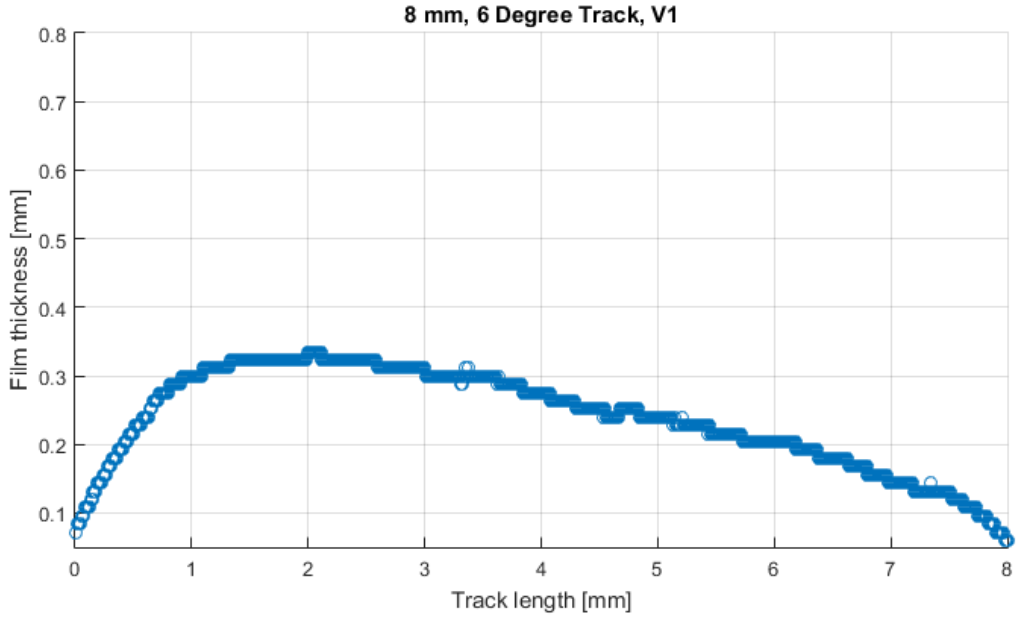

(a)

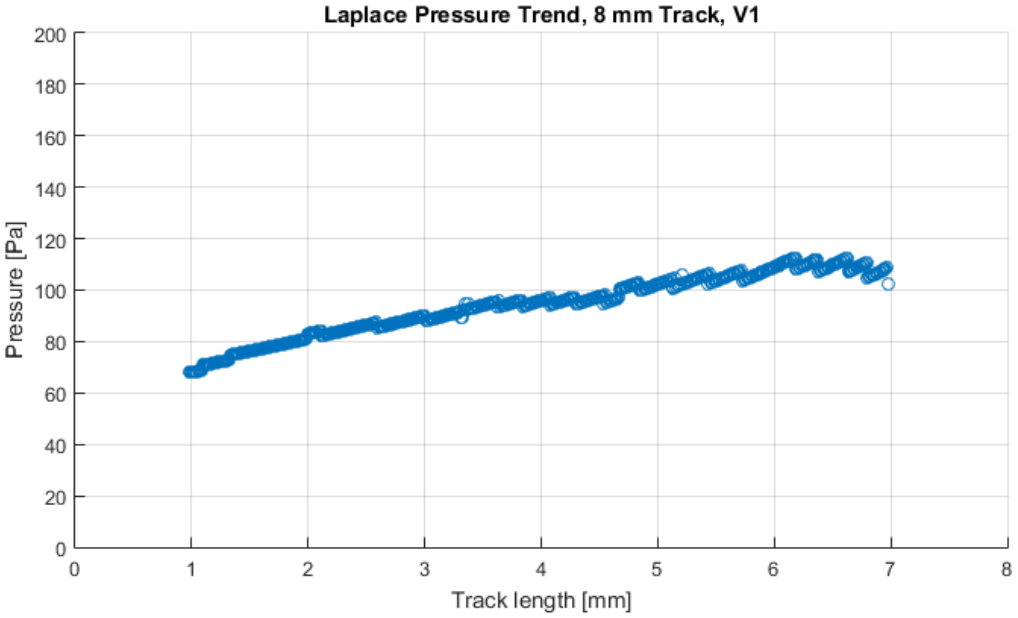

(b)

Figure 23: Water film thickness distribution (a) and Laplace pressure variation (b) for a wedge-shaped 8 mm long track, low volume case. The narrow end of the track is on the right.

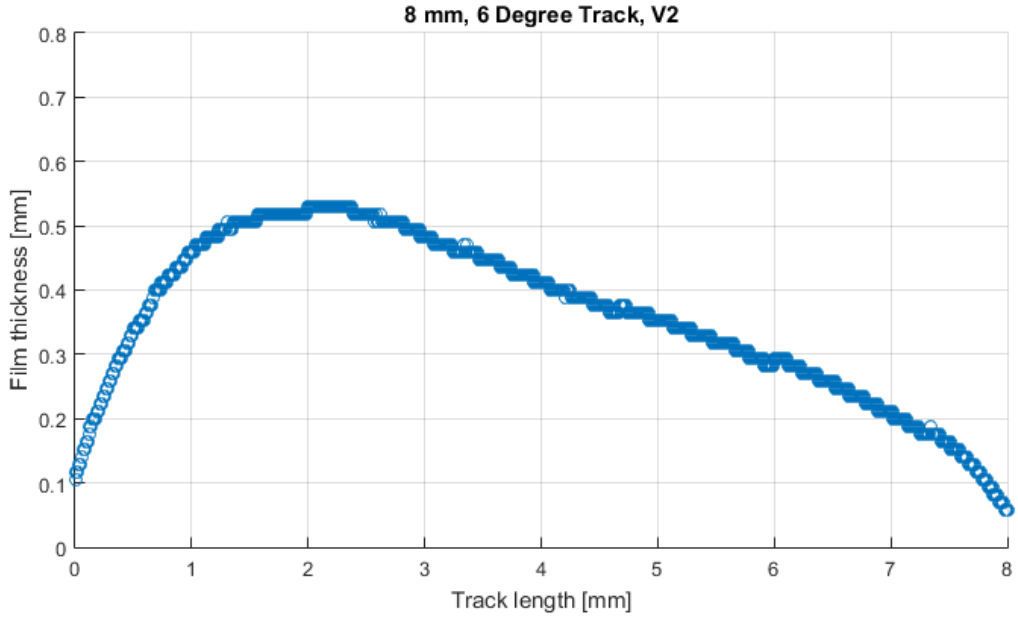

(a)

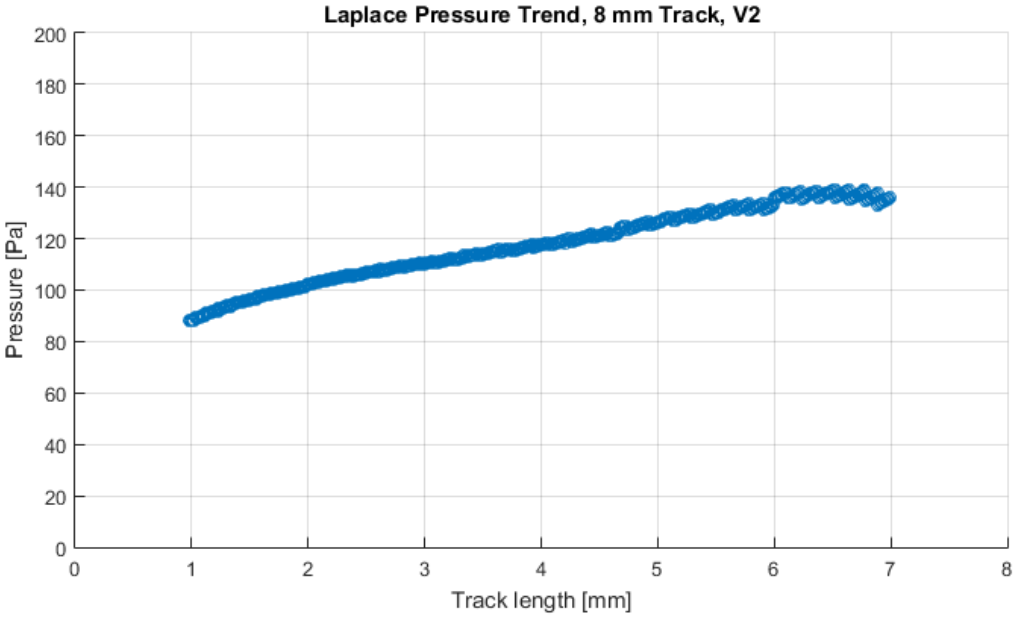

(b)

Figure 24: Water film thickness distribution (a) and Laplace pressure variation (b) for a wedge-shaped 8 mm long track, high volume case. The narrow end of the track is on the right.

Both tracks have the same end width, smaller than the capillary length of water, but different starting widths owing to their different lengths. The thickness of the liquid film was quantfied vs. length using the previously described method and subsequently digitized using image processing on Matlab (Mathworks®).

The Matlab codes in Appendix A are referred to the study conducted with oil, nevertheless these have also been used for the analysis of water with a slight modification in the dimension of the tracks and the surface tension values, when necessary.

The volume of water dispensed on each track has been computed by approximating the transverse section of the liquid as a circular segment, with its height smaller than half the track width, which here is considered to be the chord of the circular segment itself. However, this hypothesis can be considered valid only if the capillary length is higher than the track width, otherwise it would not be possible to compute the transversal area of the oil due to the flattening effect of gravity, which would distort the circular shape of the film.

The values for the Laplace pressure have been computed following the equation given by Ghosh et al. [7] and considering the longitudinal curvature of the film to be negligible compared to the transverse.

Two different cases have been explored by increasing the volume of liquid on the tracks in order to visualize the different pressure trend between them; the results obtained are presented in Figure 21, Figure 22, Figure 23 and Figure 24. First of all, by looking at the first two graphs with the lower amount of volume and neglecting the end effects of the tracks, the longest track is subjected to a Laplace pressure gradient of about 6.3 $\frac{Pa}{mm}$, a value which is clearly higher

compared to the 4 $\frac{Pa}{mm}$ obtained for the shortest one.

This is attributed to the larger volume of water present on the longer track, which has to be balanced by a higher pressure gradient as explained before.

Furthermore, the subsequent comparison between the same tracks, onto which a greater volume of liquid is dispensed, shows once again a higher increase in the absolute value of the Laplace pressure and the pressure gradient along x for the longest track (8.3 $\frac{Pa}{mm}$) than the shortest one (6.7 $\frac{Pa}{mm}$). This trend can be explained by taking into account the major role gravity plays in the second case, leading to the rise of the Laplace pressure in the narrow side of the track needed to balance the gravity force.

Moreover, since the thickness decreases towards the narrow side of the track, an increase in the radius of curvature and thus a decrease in pressure would be expected if the width remained constant; nevertheless, the track width diminishes because of the wedge angle, therefore the rise in pressure and a reduction in the curvature radius are obtained as a consequence.

Globally, the further away we move from the capillary length (for clean water and air at standard temperature and pressure, the capillary length is around 2.7 mm), the sharper the effect of gravity is, a behavior that is always valid, expecially when liquids with low κ^{-1} values are employed.

5.2 Experimental results

The previously mentioned approximation has been hereafter utilized to compute the volume of oil dispensed on the superoleophilic tracks. The capillary length for the silicone oil here

utilized is equal to 1.48 mm, therefore the tracks width has been designed according to this limit value.

The additional volume underneath the oil film captured by the camera, which is not visible

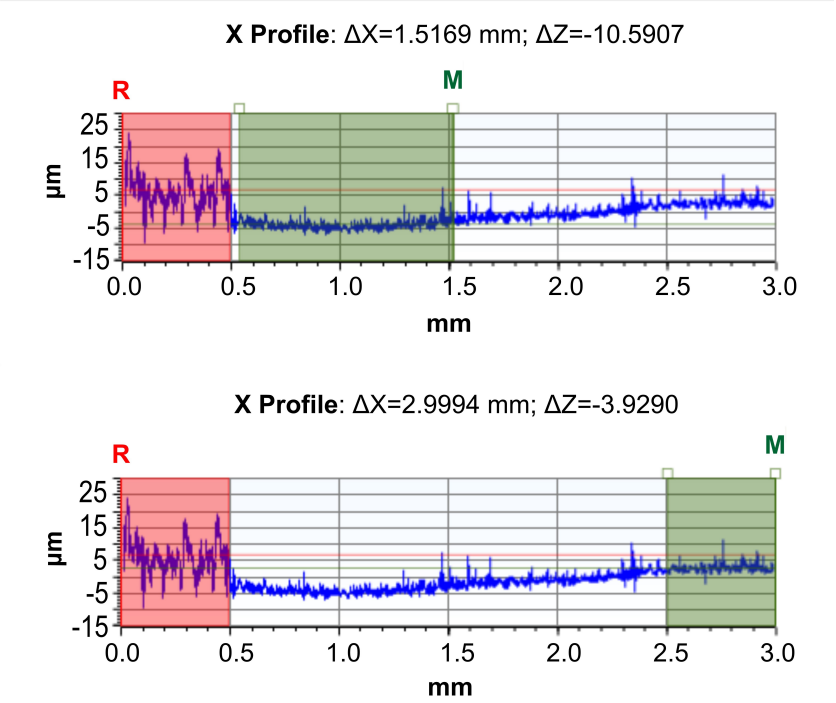

Figure 25: Step height between coating (pink shaded) and etched track measured by an optical profilometer

because of the step between the etched track and the coated substrate, has been computed after having tested one sample with a profilometer (Figure 25).

For the two portions of the etched track closer to the coated substrate (the ending part of the track is not depicted due to symmetry), the latter represented by the red shadow on the left from 0 to 0.5 mm (beginning of the track), the profilometer shows an average height value of about 10.59 μm, which is due to the higher energy supplied by the laser on the surface, caused by the beam's deceleration during the longitudinal movement towards the end of the track. When the profilometer is far away from the coated substrate ($\Delta x = 3mm$), a stabilization of the height is observed and a lower value of about 3.93 μm is achieved.
Hence, by considering the average between the two, an approximate value of about 7 μm has been utilized for the calculation of the additional liquid volume. Nevertheless, by comparing all the volumes on every track tested, a $\sim 5\%$ maximum increase in volume has been obtained, which can be neglected as a small experimental error.

The results obtained from the experimental analysis are shown in Figure 26 and Figure 27. The experiments have been conducted multiple times to check their repeatability and thus, for the sake of space conservation, the main set of results is hereafter presented, while the other two sets can be found in Appendix B.

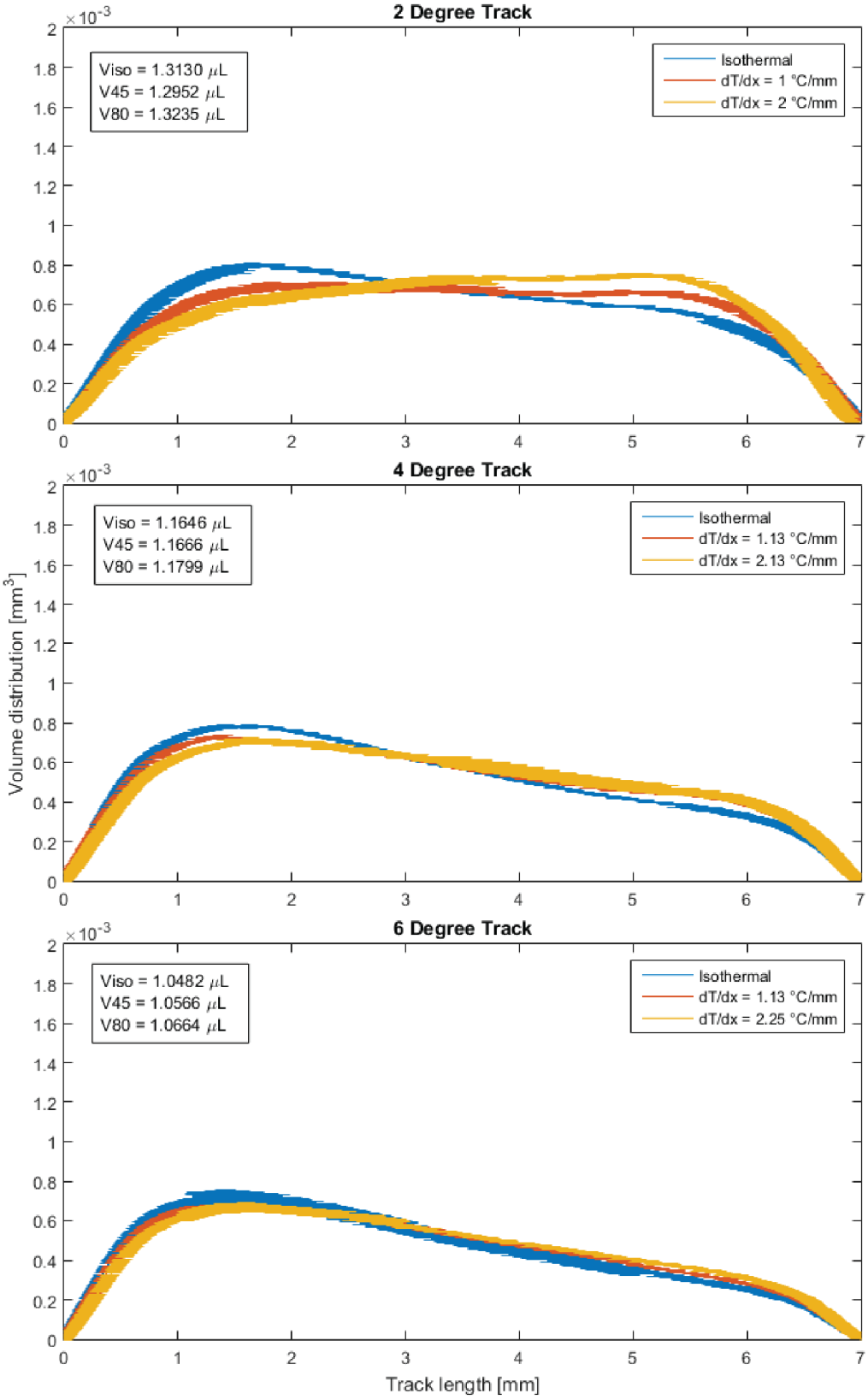

Figure 26: Film volume distribution along the track length for wedge-shaped tracks

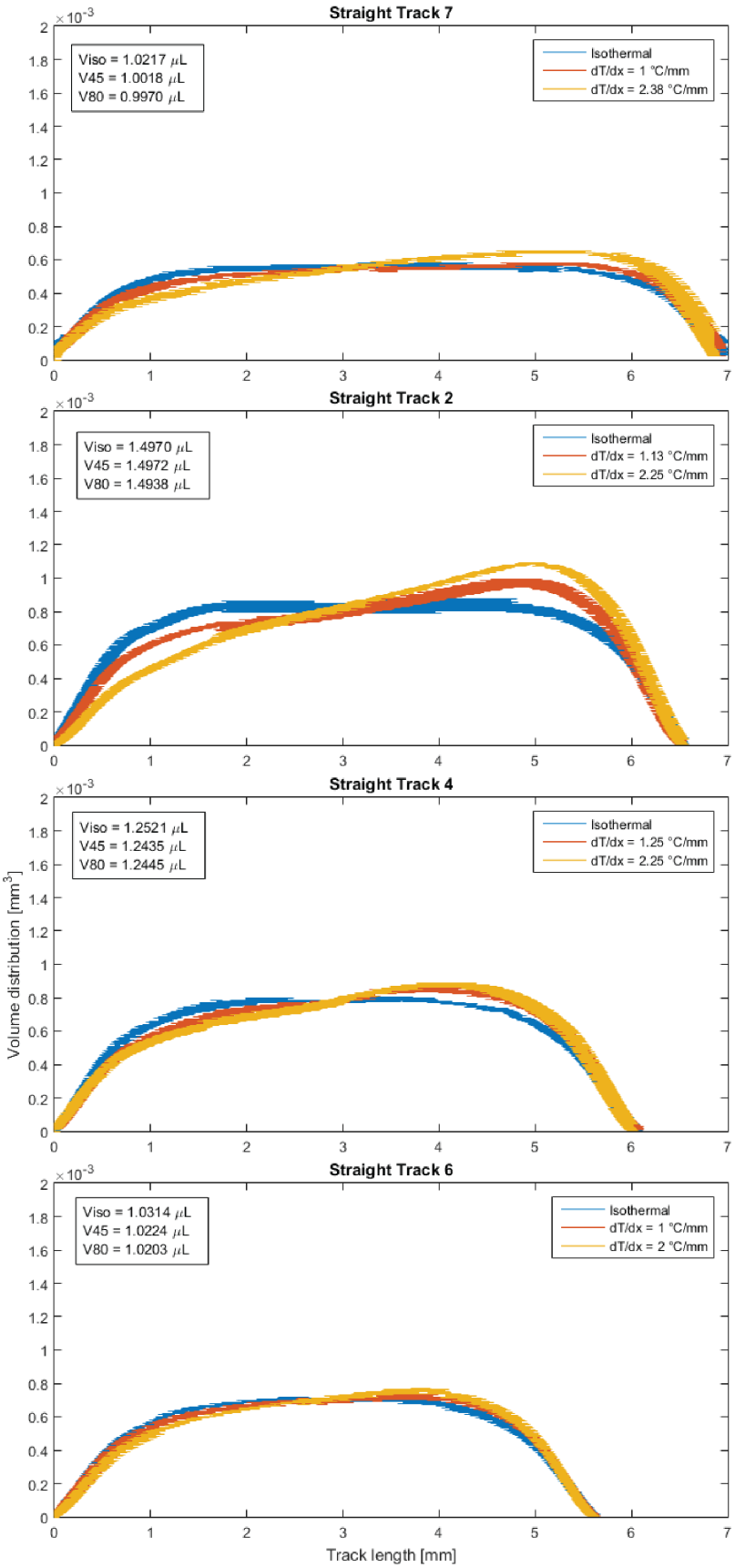

Figure 27: Film volume distribution along the track length for straight tracks

The graphs depict the oil volume distribution along the wedge-shaped and straight tracks etched on the oleophobic steel samples, for three different thermal cases, showing the change in the liquid's shape due to the variation of its surface tension caused by a change in the temperature along the longitudinal direction of the plate.

First of all, the oil volume has been calculated for each thermal case as an average of three different sets of data acquired from the image processing on Matlab, by taking into account the standard deviation and plotting the consequent error bars. In the plots, Viso stands for the volume of oil in the isothermal case, V45 represents the volume computed during the intermediate case, and V80 is the final volume value calculated when the highest temperature gradient is applied to the system, hence when the hot micro module is working at its maximum temperature of $80°C$.

The aim of the procedure described is to demonstrate that no oil evaporation occurred from the isothermal to the extreme non-isothermal case where the highest temperature on the hot side of the plate is achieved, a result that has been obtained and confirmed by the volume values computed in all of the three different thermal cases.

The volume difference between the various cases analyzed is due to the error in the accuracy when dispensing the oil by means of the micro pipette, as it was explained in the previous paragraph.

The purpose of plotting the graphs with error bars is to take into account the error due to the image processing on Matlab, which requires a very precise method to elaborate the pictures taken with the camera.

The values of the temperature gradients applied to the system affect the shape of the oil film by modifying its surface tension and creating a shear stress that leads to the movement of the liquid towards the cold side (right side). The following equation is employed in order to explain this behavior:

$$\tau_x = \frac{d\gamma}{dx} = \frac{d\gamma}{dT}\frac{dT}{dx} \tag{5.1}$$

where the first term is constant for the temperature range here considered and equal to -0.06 $\frac{mN}{m \cdot K}$ [12], while the second term is also constant since the temperature difference between the two sides of the plate is maintained fixed in each of the three thermal cases.
Hence, the highest temperature gradient creates a higher thermocapillary stress that disrupts the curvature of the liquid in a sharper way with respect to the intermediate case, thus more fluid is moved to the right where the value of γ is higher.

For the three wedge-shaped tracks, a Laplace pressure difference arises between the two ends of the track in order to balance the effect of gravity acting on the side with the highest amount of volume (left side). Hence, according to the principle of minimization of energy, the liquid acquires the shape shown by the blue line, which stands for the isothermal case.

By looking at Equation (2.1), the pressure variation is a function of the wedge angle α, therefore a higher pressure contribution and a steeper profile of the isothermal curve is found in the 4° and 6° tracks.
Knowing the angle of the circular segment, the radius of the circle the segment is part of and the thickness of the segment itself, the exposed surface area of the oil film has been computed;

moreover, knowing the temperature gradient for each case examined and the constant value of $\frac{d\gamma}{dT}$ previously mentioned, the shear stress acting on the fluid has been evaluated.

From these values of surface area and shear stress, forces of 1.16 μN, 1.23 μN and 1.30 μN have been obtained for the 2°, 4° and 6° track respectively.

Accordingly, despite the gravity force supports the shear stress in moving the oil from the hot to the cold side, the greater pressure difference encountered in these two cases reduces the global thermocapillary effect.

Moreover, this result is also proved by looking at the temperature gradient values for the three wedge-shaped tracks: even though a higher value is found for the last two cases (2.13 $\frac{^\circ C}{mm}$ and 2.25 $\frac{^\circ C}{mm}$ for the 4° and 6° track respectively) with respect to the first one (2 $\frac{^\circ C}{mm}$), still the thermocapillary force is strongly opposed by the Laplace pressure, which further validates the previously described behavior.

The results obtained with the straigth tracks show a similar trend to the one previously discussed, when comparing the three different cases having the same area of the correspondent wedge-shaped ones. Moreover, an additional test run on a track with the same length of the wedge-shaped ones has been also conducted.

No Laplace pressure difference is here observed when considering the isothermal case, due to the constant width of the tracks, thus the shear stress created is seemingly only balanced by the gravity force acting on the film, resulting in a sharper observed effect.

The distortion of the film shape due to the increase in temperature leads to a subsequent decrease in the surface tension on both track ends, as well as to a rise in the radius of curvature

on the hot side, due to the flattening of the oil, and a decrease in the radius of curvature on the cold side.

By looking at the representative graphs for the straight track 2 shown in Figure 28, a decrease in the pressure is seen on the hot side of the track, while a constant value of pressure is observed on the opposite side, thus leading to a significant pressure difference along the x direction.

According to this, the thermocapillary effect is now counterbalanced both by the pressure and the gravity force, a behavior which differs from the one pertinent to the wedge-shaped tracks, for which the effect of gravity is beneficial for the thermocapillarity.

Despite this, the effect of the Laplace pressure is still greater on the film placed on the wedge-shaped tracks with respect to the straight ones, thus proving the fact that a lower amount of fluid is displaced from the hot to the cold side in the first case.

Lastly, by looking at all the graphs representing the volume distribution over a straight track, we observed a lower movement of the oil when the length of the track was reduced, a behavior that can be explained by analyzing the Bond number, which represents the ratio of gravitational force to surface tension force:

$$Bo = \frac{\Delta \rho g L^2}{\gamma} \tag{5.2}$$

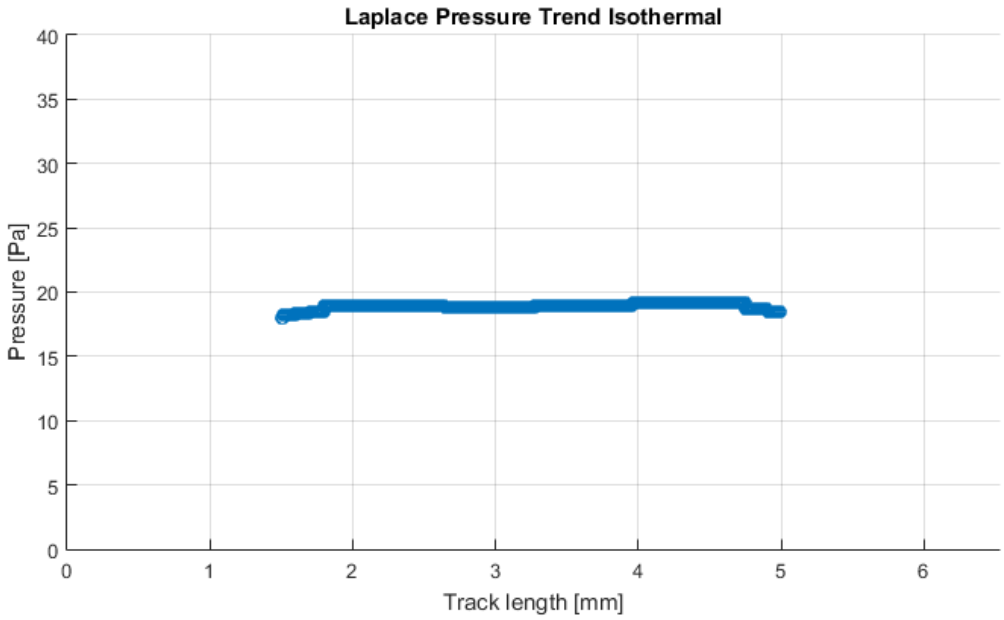

(a)

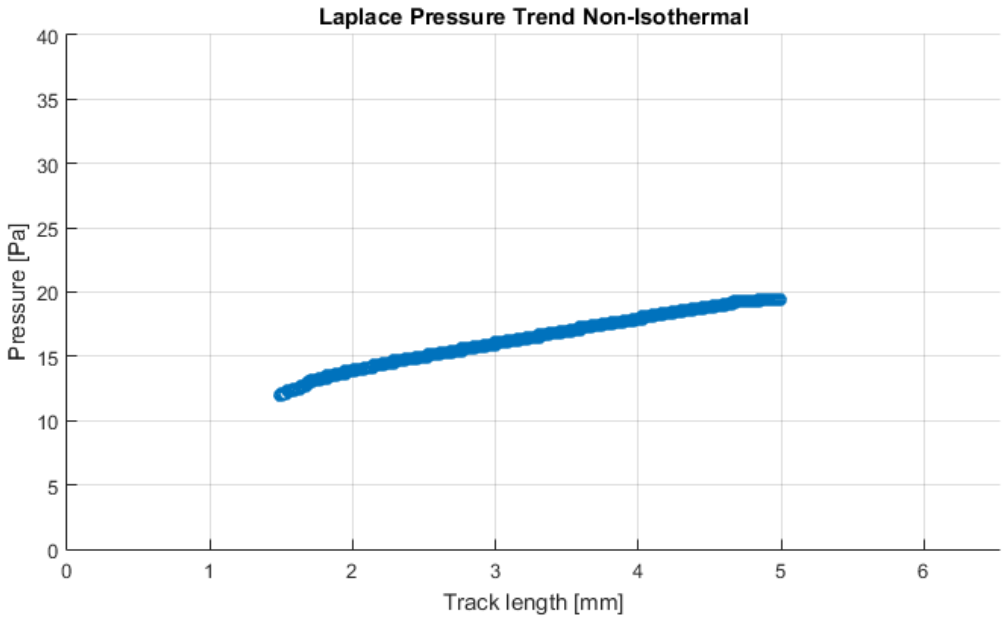

(b)

Figure 28: Isothermal (a) and non-isothermal (b) Laplace pressure trend for a straight track

where $\Delta\rho$ is the difference between the liquid and the air density, L is the characteristic length which, in this case, corresponds to the track length and γ is the surface tension of the liquid.

Since the effect of the reduction in length is amplified by the squared term placed at the numerator of the equation, and knowing that the changes in γ are negligible compared to its value, the surface tension force dominates over the gravitational one, thus decreasing the Bond number and preventing other forces from taking effect.

CHAPTER 6

CONCLUSION

The thermocapillary effect, a phenomenon deriving from a gradient in the surface tension of a liquid when a change in the temperature is applied to the system, has been studied both theoretically and experimentally, in order to visualize the mass transfer of a fluid along specific wettability-confined tracks and understand the interplay between the forces acting in this micro scale application.

For this purpose, the work done by previous researchers on the transport of fluids on super-oleophilic wedge-shaped tracks, driven solely by the capillary force, has been studied in order to reproduce the optimal condition needed for the experiments conducted. A particular type of steel (AISI 1018) has been chosen as a substrate onto which a specific silicone oil, characterized by a low surface tension and low volatility (which keep it free of surfactants contamination), has been placed.

A formulation based on TiO_2 nanoparticles, PMC copolymer, ethanol and acetic acid has been created by using different mass fractions, in order to achieve the best oleophobic structure on to the metallic substrate, which has been subsequently laser-etched to create the two types of tracks where the liquid has been dispensed (wedge-shaped and straight tracks).
Hence, the confinment between the track and the coated substrate has been achieved, after a multitude of tests, which have shown good results even when different types of liquid have been employed.

The experimental setup has been designed to accomodate the sample and the micro modules working according to the Peltier effect, one used to supply heat to the plate and the other one to cool it down, and assembled in order to minimize the thermal losses by using appropriate insulating materials.

A preliminary experiment has been conducted to validate the assumption of negligible temperature gradients along the transverse and vertical direction of the sample, thus allowing a one-dimensional analysis of the system by simply taking into account the temperature gradient imposed along the longitudinal direction of the track.

Afterwards, all the experiments have been conducted and the results processed using the software Matlab, by means of which it has been possible to map the behavior of the oil for three different thermal states. The tendency of the fluid to move towards the region where the surface tension is higher has been observed; however, for wedge-shaped tracks, the distortion of the shape of the liquid is clearly less sharp than for straight tracks, due to the additional effect of the Laplace pressure which counteracts the thermocapillary effect.

When comparing straight tracks with different lengths, a small distortion of the shape of the fluid is ascertained for the shortest track, suggesting that the surface tension force plays a stronger role than the gravitational one, thus preventing other forces from taking effect.

In conclusion, further work is needed to better explore the effect of the track length on the distortion of the oil film, which clearly plays an important role when high volumes of oil are dispensed on the tracks. Moreover, a fixed amount of volume could be placed on the tracks using

alternative methods, in order to study the influence of the film thickness on the effectiveness of the thermocapillary effect to induce mass transfer of a fluid.

APPENDICES

Appendix A

MATLAB CODES

A.1 Code for image processing

```
% Single image
% Film thickness distribution on wedge-shaped track


close all
clear all
I = imread('2deg_80h10c_a.jpg');
figure
imshow(I)
[x,y] = ginput(2);
level = graythresh(I);
bw = im2bw(I, level);      % Light intensity = 90


I2 = imread('2deg_80h10c_b.jpg');
figure
imshow(I2)
[x2,y2] = ginput(2);
```

Appendix A (continued)

```
level = graythresh(I);
bw2 = im2bw(I2, level);

I3 = imread('2deg_80h10c_c.jpg');
figure
imshow(I3)
[x3,y3] = ginput(2);
level = graythresh(I);
bw3 = im2bw(I3, level);

I4 = imread('2deg_80h10c_d.jpg');
figure
imshow(I4)
[x4,y4] = ginput(2);
level = graythresh(I);
bw4 = im2bw(I4, level);

close all

% Indicate substrate/track length and create substrate line
% for each figure
```

Appendix A (continued)

```
% Fig1
x(1) = round(x(1));
x(2) = round(x(2));
y(1) = round(y(1));
y(2) = y(1);
X = zeros(1,x(2)-x(1)+1);
X(1) = x(1);
Y = y(1);
L1 = zeros (1,x(2)-x(1)+1);

for n=1:(x(2)-x(1)+1)
    X(n)= X(1) + n-1;
end

maxX = size(X);
maxX = maxX(2);

% Fig2
x2(1) = round(x2(1));
x2(2) = round(x2(2));
```

Appendix A (continued)

```
y2(1) = round(y2(1));

y2(2) = y2(1);

Y2 = y2(1);

X2 = zeros(1,x2(2)-x2(1)+1);

X2(1) = x2(1);

L1_2 = zeros (1,x2(2)-x2(1)+1);


for n = 1:(x2(2)-x2(1)+1)

    X2(n) = X2(1) + n-1;

end


maxX_2 = size(X2);

maxX_2 = maxX_2(2);


% Fig3

x3(1) = round(x3(1));

x3(2) = round(x3(2));

y3(1) = round(y3(1));

y3(2) = y3(1);

Y3 = y3(1);

X3 = zeros(1,x3(2)-x3(1)+1);
```

Appendix A (continued)

```
X3(1) = x3(1);

L1_3 = zeros (1,x3(2)-x3(1)+1);


for n = 1:(x3(2)-x3(1)+1)

    X3(n) = X3(1) + n-1;

end


maxX_3 = size(X3);

maxX_3 = maxX_3(2);


% Fig4

x4(1) = round(x4(1));

x4(2) = round(x4(2));

y4(1) = round(y4(1));

y4(2) = y4(1);

Y4 = y4(1);

X4 = zeros(1,x4(2)-x4(1)+1);

X4(1) = x4(1);

L1_4 = zeros (1,x4(2)-x4(1)+1);


for n = 1:(x4(2)-x4(1)+1)
```

Appendix A (continued)

```
    X4(n) = X4(1) + n-1;
end


maxX_4 = size(X4);
maxX_4 = maxX_4(2);


% Scan for film thickness along previously defined length of track


% Fig1
for l = 1:(x(2)-x(1)+1)


for k = 1:maxX
   BW = bw(Y-k,X(l));
    if BW > 0
        L1(l) = k-1;
    break
    else L1(l) = 0;
    end
end
end
```

Appendix A (continued)

```
% Fig2
for l = 1:(x2(2)-x2(1)+1)

for k = 1:maxX_2
    BW2 = bw2(Y2-k,X2(l));
    if BW2 > 0
        L1_2(l) = k-1;
    break
    else L1_2(l) = 0;
    end
end
end

% Fig3
for l = 1:(x3(2)-x3(1)+1)

for k = 1:maxX_3
    BW3 = bw3(Y3-k,X3(l));
    if BW3 > 0
        L1_3(l) = k-1;
    break
```

Appendix A (continued)

```
    else L1_3(l) = 0;
    end
end
end

% Fig4
for l = 1:(x4(2)-x4(1)+1)

for k = 1:maxX_4
    BW4 = bw4(Y4-k,X4(l));
    if BW4 > 0
        L1_4(l) = k-1;
    break
    else L1_4(l) = 0;
    end
end
end

% Join the 4 vectors

Length_test = (x(2)-x(1)) + (x2(2)-x2(1)) + (x3(2)-x3(1)) +...
```

Appendix A (continued)

```
(x4(2)-x4(1));

scale_test = 7 / Length_test;

Xtot_test = 0:1:Length_test;

Xtot_test = Xtot_test .* scale_test;


L1 = L1(1:end-1);

L1_2 = L1_2(1:end-1);

L1_3 = L1_3(1:end-1);


L = [L1';L1_2';L1_3';L1_4'];

plot(Xtot_test,L*scale_test)

axis([0 7 0 1.5])


% Volume calculation


Ln = numel(L);

scale_new = 7 / Ln ;

scale_new_cub = scale_new^3;

L_pix = L;

C = zeros(1,Ln);

R = zeros(1,Ln);
```

Appendix A (continued)

```
theta = zeros(1,Ln);

Rsq = zeros(1,Ln);

Aincr = zeros(1,Ln);


% Calculate track width along same length


Xtrack = 0:1:Ln ;

Xend = 0.74 / scale_new ;  % = [pixels] (Rend = 0.74 mm)

Xend = round(Xend);

Xbeg = 0.63 / scale_new;   % = [pixels] (Rbeg = 0.63 mm)

Xbeg = round(Xbeg);


for o = 1:(Xend+1)

    C(o) = sqrt((Xend-(Xtrack(o)/2))*8*Xtrack(o));

end


for j = (Xend+2):(Ln-Xbeg)

    C(j) = C(Xend+1) - ((2*(j-(Xend+2)))/tand(89)) ;

end


for q = (Ln-Xbeg+1):(Ln+1)
```

Appendix A (continued)

```
 C(q) = sqrt((Xbeg-((Xtrack(Ln+1)-Xtrack(q))/2))*8*(Xtrack(Ln+1)...
      -Xtrack(q)));
end


C = C .* scale_new;
Csq = power(C,2);
L_pix = L_pix .* scale_new;


for s = 1:Ln
     R(s) = (L_pix(s)/2) + (Csq(s)/(8*L_pix(s)));
     theta(s) = 2*asin(C(s)/(2*R(s)));
     Rsq(s) = R(s)^2;
     Aincr(s) = (Rsq(s)/2)*(theta(s)-sin(theta(s)));
end


Vincr = Aincr .* scale_new;


L_pix
C/2
Vol = sum(Vincr)
```

Appendix A (continued)

```
%% Laplace pressure for isothermal case
LP = zeros(1,Ln);

for s = 1:Ln
     R(s) = R(s)*0.001;
    LP(s) = 0.0213/R(s);   %constant at isothermal 16 C
end

%% Laplace pressure for non-isothermal case
LP = zeros(1,Ln);
gama = zeros(1,Ln);
Temp = zeros(1,Ln);

for s = 1:Ln
     R(s) = R(s)*0.001;
     Temp(s) = -2.077*Xtot_test(s) + 67.3125;
     gama(s) = 20.8  -0.06*(Temp(s)-25);
     gama(s) = gama(s)*0.001;
     LP(s) = gama(s)/R(s);
end
```

Appendix A (continued)

```
figure
scatter(Xtot_test,LP)


% Surface area calculation
sum(R .*theta)*scale_new
```

A.2 Code for the final analysis

```
%% Final analysis of the oil film


Lone = L*scale_new;
Xtot_1 = Xtot_test;
Lavg_firstset = mean(Lone);
StdDev1 = std(Vincr);
Vavg1 = Vincr;
V1 = Vol;
LP1 = LP;


%%
Ltwo = L*scale_new;
Xtot_2 = Xtot_test;
Lavg_secondset = mean(Ltwo);
```

Appendix A (continued)

```
StdDev2 = std(Vincr);

Vavg2 = Vincr;

V2 = Vol;

LP2 = LP;


%%

Lthree = L*scale_new;

Xtot_3 = Xtot_test;

Lavg_thirdset = mean(Lthree);

StdDev3 = std(Vincr);

Vavg3 = Vincr;

V3 = Vol;

LP3 = LP;


%% Fix the length of the vectors for the graph

length = [max(size(Lone)) max(size(Ltwo)) max(size(Lthree))];

x_axis = [max(size(Xtot_1)) max(size(Xtot_2)) max(size(Xtot_3))];

Vincr_Vec = [max(size(Vavg1)) max(size(Vavg2)) max(size(Vavg3))];

LP_var = [max(size(LP1)) max(size(LP2)) max(size(LP3))];


if length(1)> min(length)
```

Appendix A (continued)

```
        Lone = Lone(1:end-(length(1)-min(length)));
end

if length(2)> min(length)
        Ltwo = Ltwo(1:end-(length(2)-min(length)));
end

if length(3)> min(length)
        Lthree = Lthree(1:end-(length(3)-min(length)));
end

%Fix the length of the x-axis
if x_axis(1)> min(x_axis)
        Xtot_1 = Xtot_1(1:end-(x_axis(1)-min(x_axis)));
end

if x_axis(2)> min(x_axis)
        Xtot_2 = Xtot_2(1:end-(x_axis(2)-min(x_axis)));
end

if x_axis(3)> min(x_axis)
```

Appendix A (continued)

```
        Xtot_3 = Xtot_3(1:end-(x_axis(3)-min(x_axis)));
end

%Fix the length of the volume vector

if Vincr_Vec(1)> min(Vincr_Vec)
        Vavg1 = Vavg1(1:end-(Vincr_Vec(1)-min(Vincr_Vec)));
end

if Vincr_Vec(2)> min(Vincr_Vec)
        Vavg2 = Vavg2(1:end-(Vincr_Vec(2)-min(Vincr_Vec)));
end

if Vincr_Vec(3)> min(Vincr_Vec)
        Vavg3 = Vavg3(1:end-(Vincr_Vec(3)-min(Vincr_Vec)));
end

%Fix the length of the pressure vector

if LP_var(1)> min(LP_var)
        LP1 = LP1(1:end-(LP_var(1)-min(LP_var)));
```

Appendix A (continued)

```
end


if LP_var(2)> min(LP_var)
        LP2 = LP2(1:end-(LP_var(2)-min(LP_var)));
end


if LP_var(3)> min(LP_var)
        LP3 = LP3(1:end-(LP_var(3)-min(LP_var)));
end


Ltot = [Lone, Ltwo, Lthree];
LAVG = [Lavg_firstset, Lavg_secondset, Lavg_thirdset];
Xtot = Xtot_3;
VAVG = [Vavg1; Vavg2; Vavg3];
LPAVG = [LP1; LP2; LP3];


StdDev = std(Ltot);
Mean = mean(Ltot');
Xavg = mean(Xtot');
StdDevAvg = std(VAVG);
MeanAvg = mean(LAVG');
```

Appendix A (continued)

```
MeanV = mean(VAVG);

MeanLP = mean(LPAVG);

Avg_Vol = (V1+V2+V3)/3


%% Plot the oil film along the track


errorbar(Xtot,MeanV,StdDevAvg)

axis([0 7 0 0.003])

title('2 Degree Track')

xlabel('Track length [mm]')

ylabel('Volume distribution [mm^3]')

legend('Isothermal')

dim = [0.2 0.5 0.3 0.3];

str = {'Viso = \muL','V45 = \muL','V80 = \muL'};

annotation('textbox',dim,'String',str,'FitBoxToText','on');


%%

hold on

errorbar(Xtot,MeanV,StdDevAvg,'DisplayName','dT/dx = C/mm')


%%
```

Appendix A (continued)

```
hold on

errorbar(Xtot,MeanV,StdDevAvg,'DisplayName','dT/dx =  C/mm')
```

Appendix B

EXPERIMENTAL GRAPHS

B.1 Second set of experiments

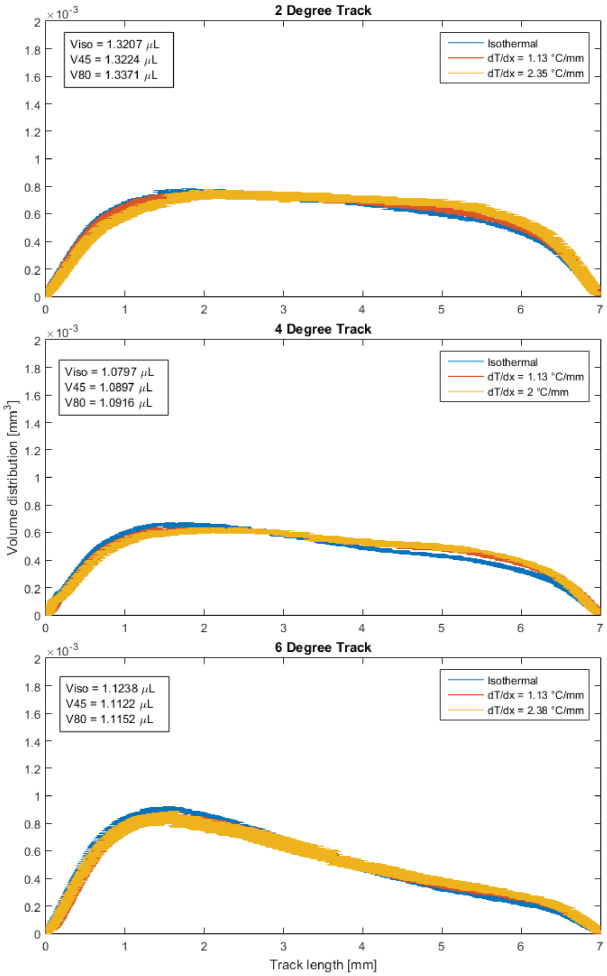

Figure 29: Film volume distribution along the track length for wedge-shaped tracks - Set 2

Appendix B (continued)

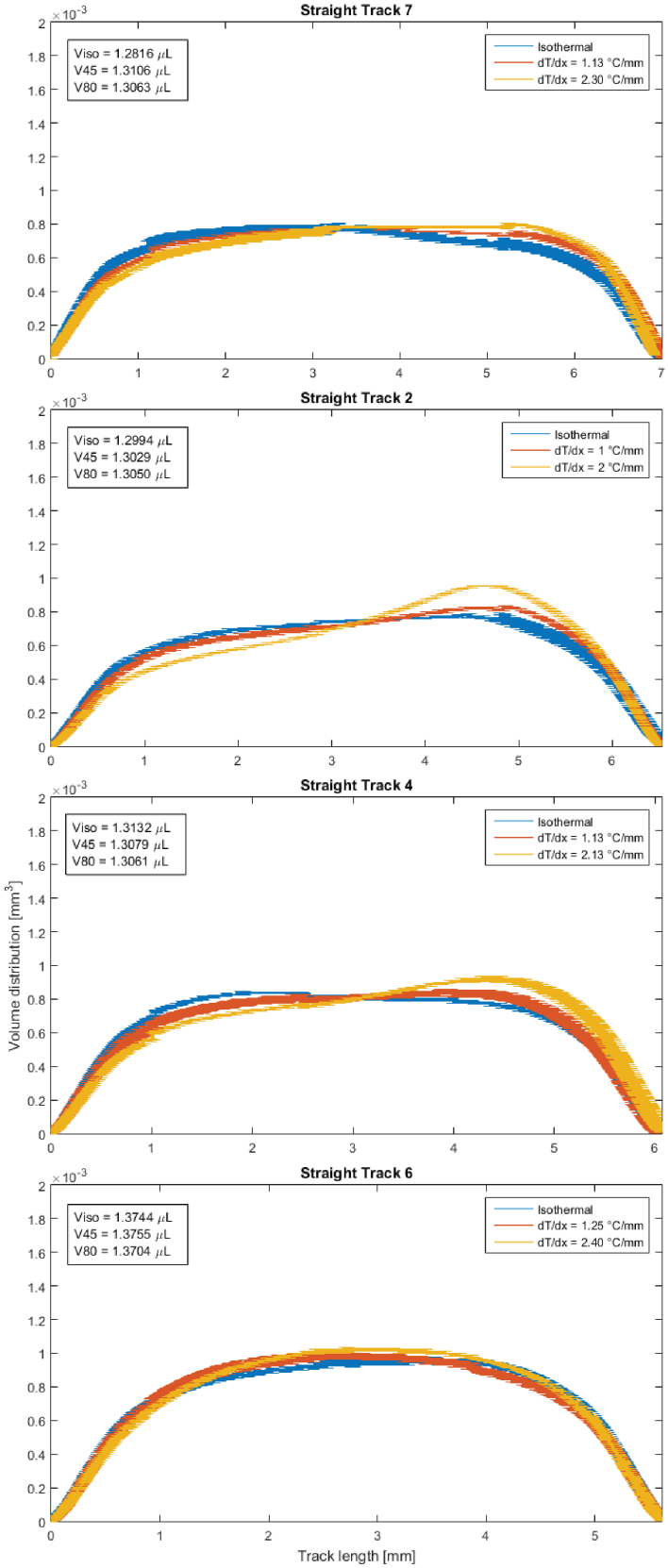

Figure 30: Film volume distribution along the track length for straight tracks - Set 2

Appendix B (continued)

B.2 Third set of experiments

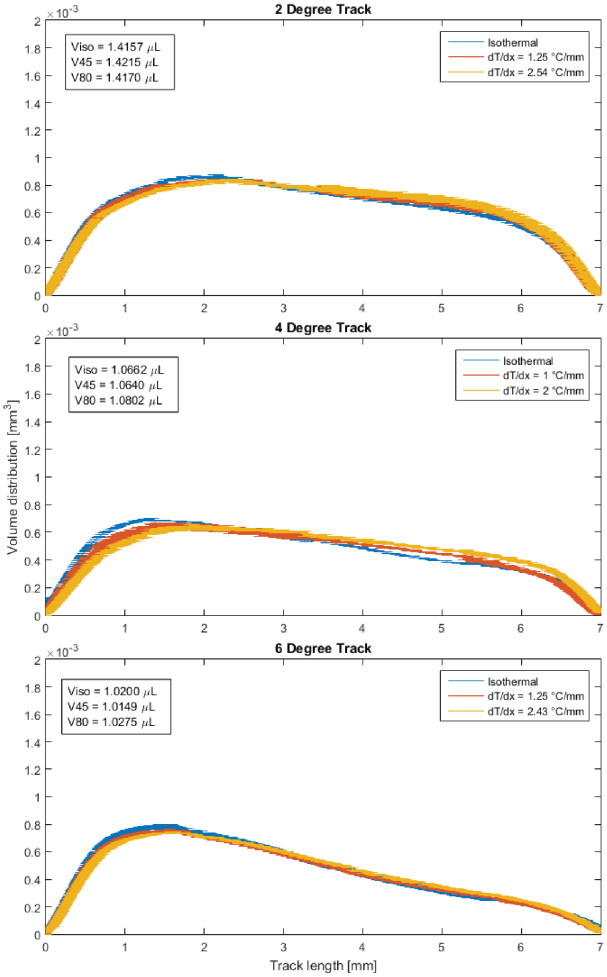

Figure 31: Film volume distribution along the track length for wedge-shaped tracks - Set 3

Appendix B (continued)

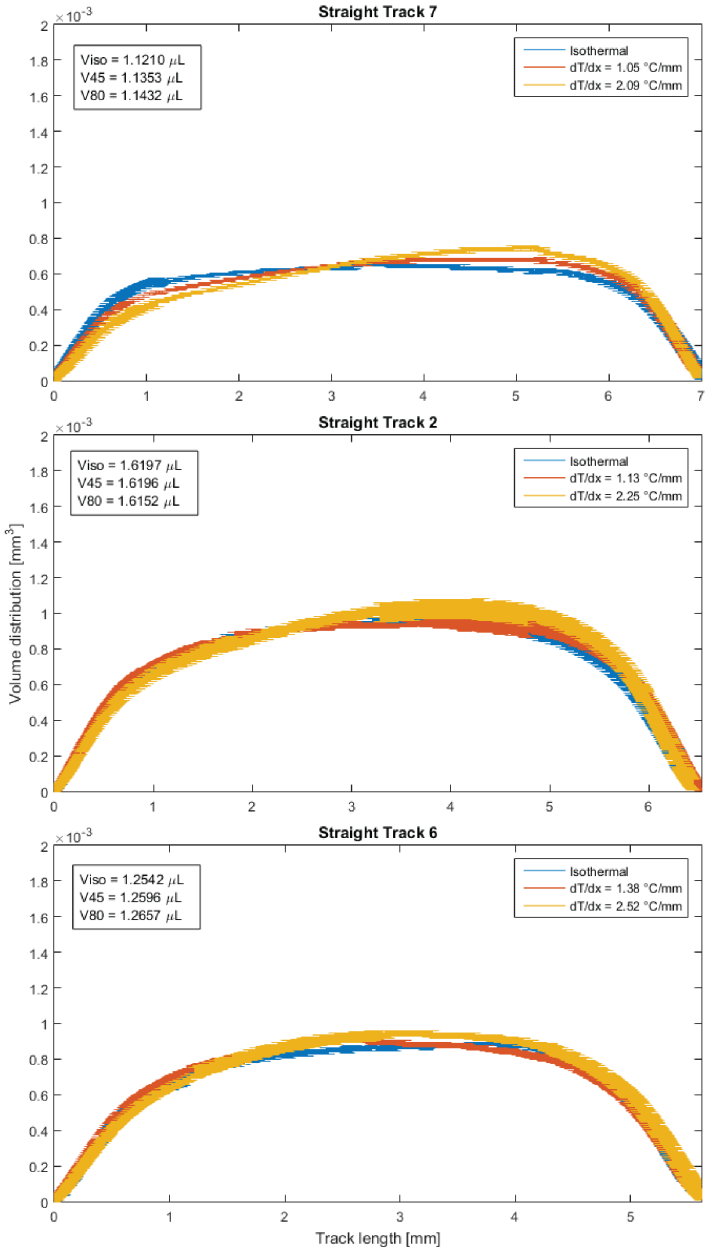

Figure 32: Film volume distribution along the track length for straight tracks - Set 3

Appendix C

AUTHORIZATION FOR IMAGE USED IN FIGURE 10

ROYAL SOCIETY OF CHEMISTRY LICENSE TERMS AND CONDITIONS

Mar 27, 2017

This Agreement between Antonio Lafratta ("You") and Royal Society of Chemistry ("Royal Society of Chemistry") consists of your license details and the terms and conditions provided by Royal Society of Chemistry and Copyright Clearance Center.

License Number	4077380295626
License date	Mar 27, 2017
Licensed Content Publisher	Royal Society of Chemistry
Licensed Content Publication	Lab on a Chip
Licensed Content Title	Wettability patterning for high-rate, pumpless fluid transport on open, non-planar microfluidic platforms
Licensed Content Author	Aritra Ghosh,Ranjan Ganguly,Thomas M. Schutzius,Constantine M. Megaridis
Licensed Content Date	Mar 13, 2014
Licensed Content Volume	14
Licensed Content Issue	9
Type of Use	Thesis/Dissertation
Requestor type	academic/educational
Portion	figures/tables/images
Number of figures/tables/images	1
Format	print and electronic
Distribution quantity	1
Will you be translating?	no
Order reference number	
Title of the thesis/dissertation	Thermocapillary Effects on Fluid Distributed on Wettability-Confined Tracks
Expected completion date	May 2017
Estimated size	100
Requestor Location	Antonio Lafratta 809 S Damen Avenue, Apt 1217A CHICAGO, IL 60612 United States Attn: Antonio Lafratta
Billing Type	Invoice
Billing Address	Antonio Lafratta 809 S Damen Avenue, Apt 1217A CHICAGO, IL 60612 United States Attn: Antonio Lafratta
Total	0.00 USD

CITED LITERATURE

1. Gennes, P. G. D., Quéré, D., and Brochard-Wyart, F.: Capillarity and Wetting Phenomena: Drops, Bubbles, Pearls, Waves. Paris, France, Springer, 2004.

2. Marmur, A.: Hydro-hygro-oleo-omni-phobic? Terminology of wettability classification. Soft Matter, 8:6867–6870, 2012.

3. Quéré, D.: Wetting and roughness. Annual Review of Materials Research, 38:71–99, 2008.

4. Oliver, J., Huh, C., and Mason, S.: Resistance to spreading of liquids by sharp edges. F. Colloid Interface Sci., 59:568–81.

5. Onda, T., Shibuichi, S., Satoh, N., and Tsujii, K.: Super-water-repellent fractal surfaces. Langmuir, 12:2125–27, 1996.

6. Shibuichi, S., Onda, T., Satoh, N., and Tsujii, K.: Super water-repellent surfaces resulting from fractal structure. F. Phys. Chem, 100:19512–17, 1996.

7. Ghosh, A., Ganguly, R., Schutzius, T. M., and Megaridis, C. M.: Wettability patterning for high-rate, pumpless fluid transport on open, non-planar microfluidic platforms. Lab Chip, 14:1538, 2014.

8. Davis, S. H.: Thermocapillary instabilities. Ann. Rev. Fluid Mech., 19:403–35, 1987.

9. Fedosov, A. I.: Thermocapillary motion. Zhurnal Fizicheskoi Khimii 30, 2:366–373, 1956.

10. Birikh, R. V.: Thermocapillary convection in a horizontal layer of liquid. Zhurnat Prikladnoi Mekhaniki i Teekhnieheskoi Fiziki, 3:69–72, 1966.

11. Barakhovskaia, E. V., Marchuk, I. V., and Fedorets, A. A.: Thermocapillary deformation in a locally heated layer of silicone oil. Journal of Physics: Conference series 754, 2016.

12. Dee, G. T. and Sauer, B. B.: The molecular weight and temperature dependence of polymer surface tension: comparison of experiment with interface gradient theory. Journal of colloid and interface science, 152(1), 1992.

VITA

NAME	Antonio Lafratta
EDUCATION	
	Master of Science, Mechanical Engineering, University of Illinois at Chicago, May 2017, USA
	Master's Degree, Mechanical Engineering, Politecnico di Torino, July 2017, Italy
	Bachelor's Degree, Mechanical Engineering, Politecnico di Torino, October 2015, Italy
WORK EXPERIENCE	
Oct 2016 - May 2017	Desk/Security worker, Campus Housing, University of Illinois at Chicago, USA
Mar 2016 - Jul 2016	Teaching assistant of Fundamentals of Thermal and Hydraulic Machines and Fluid Power, Politecnico di Torino, Italy
Mar 2015 - Oct 2015	Computer lab assistant, Politecnico di Torino, Italy
HONORS	
	TOP-UIC Scholarship for double degree program between Politecnico di Torino and University of Illinois at Chicago, 2016
LANGUAGE SKILLS	
Italian	Native speaker
English	Full working proficiency
French	Elementary proficiency
German	Elementary proficiency